The Cryosphere, 19, 619–644, 2025
https://doi.org/10.5194/tc-19-619-2025

The Cryosphere Open Access EGU

Formation and fate of freshwater on an ice floe in the Central Arctic

Madison M. Smith[1], Niels Fuchs[2], Evgenii Salganik[3], Donald K. Perovich[4], Ian Raphael[4], Mats A. Granskog[3], Kirstin Schulz[5], Matthew D. Shupe[6,7], and Melinda Webster[8]

[1]Applied Ocean Physics and Engineering, Woods Hole Oceanographic Institution, Woods Hole, Massachusetts, USA
[2]Institute of Oceanography, Universität Hamburg, Hamburg, Germany
[3]Norwegian Polar Institute, Fram Centre, Tromsø, Norway
[4]Thayer School of Engineering, Dartmouth College, Hanover, NH, USA
[5]Oden Institute for Computational Engineering and Sciences, The University of Texas at Austin, Austin, TX, USA
[6]CIRES, University of Colorado Boulder, Boulder, CO, USA
[7]NOAA Physical Sciences Laboratory, Boulder, CO, USA
[8]Polar Science Center, Applied Physics Laboratory, University of Washington, Seattle, WA, USA

Correspondence: Madison M. Smith (madisonmsmith@whoi.edu)

Received: 28 June 2024 – Discussion started: 9 July 2024
Revised: 3 December 2024 – Accepted: 4 December 2024 – Published: 7 February 2025

Abstract. The melt of snow and sea ice during the Arctic summer is a significant source of relatively fresh meltwater. The fate of this freshwater, whether in surface melt ponds or thin layers underneath the ice and in leads, impacts atmosphere–ice–ocean interactions and their subsequent coupled evolution. Here, we combine analyses of datasets from the Multidisciplinary drifting Observatory for the Study of Arctic Climate (MOSAiC) expedition (June–July 2020) for a process study on the formation and fate of sea ice freshwater on ice floes in the Central Arctic. Our freshwater budget analyses suggest that a relatively high fraction (58 %) is derived from surface melt. Additionally, the contribution from stored precipitation (snowmelt) outweighs by 5 times the input from in situ summer precipitation (rain). The magnitude and rate of local meltwater production are remarkably similar to those observed on the prior Surface Heat Budget of the Arctic Ocean (SHEBA) campaign, where the cumulative summer freshwater production totaled around 1 m during both. A relatively small fraction (10 %) of freshwater from melt remains in ponds, which is higher on more deformed second-year ice (SYI) compared to first-year ice (FYI) later in the summer. Most meltwater drains laterally and vertically, with vertical drainage enabling storage of freshwater internally in the ice by freshening brine channels. In the upper ocean, freshwater can accumulate in transient meltwater layers on the order of 0.1 to 1 m thick in leads and under the ice. The presence of such layers substantially impacts the coupled system by reducing bottom melt and allowing false bottom growth; reducing heat, nutrient, and gas exchange; and influencing ecosystem productivity. Regardless, the majority fraction of freshwater from melt is inferred to be ultimately incorporated into the upper ocean (75 %) or stored internally in the ice (14 %). Terms such as the annual sea ice freshwater production and meltwater storage in ponds could be used in future work as diagnostics for global climate and process models. For example, the range of values from the CESM2 climate model roughly encapsulate the observed total freshwater production, while storage in melt ponds is underestimated by about 50 %, suggesting pond drainage terms as a key process for investigation.

1 Introduction

During the Arctic summer, sea ice melt and snowmelt provide a substantial source of relatively fresh water. Precipitation provides an additional source of freshwater during the melt season that is typically small. Meltwater can accumulate in surface or subnivean melt ponds and in brine channels within the ice or drain to the ocean, where it may accumulate in layers under the ice or in leads, become separated from the ocean below by a sharp halocline (e.g., Smith et al., 2022b; Salganik et al., 2023a; Smith et al., 2023), or be directly incorporated into the upper ocean. The magnitude and fate of

freshwater associated with sea ice melt are important for the surface energy budget, ice mass balance, ocean structure, and primary productivity, as described below.

Examination of freshwater budgets from prior observational efforts suggested that most freshwater is generated by sea ice surface melt and bottom melt (Perovich et al., 2021), driven primarily by atmospheric and oceanic heat, respectively. Observations over the past few decades have suggested a shift in partitioning between surface melt and bottom melt, with bottom melt increasing more rapidly (Perovich and Richter-Menge, 2015). Partitioning varies regionally, with slightly more bottom melt than surface melt observed across most of the Arctic Basin. The representation of sea ice melt in global climate models similarly suggests that bottom melt is historically a larger budget term than surface melt (Keen et al., 2021).

Melt ponds form during the summer melt season from the pooling of snow and surface sea ice melt. Their temporal evolution and morphology are controlled by surface topography (Fetterer and Untersteiner, 1998; Petrich et al., 2012; Polashenski et al., 2012; Webster et al., 2015). The seasonal evolution of melt ponds has been a focus of study in recent years due to their significant role in the summer heat budget, primarily through reducing the surface albedo and increasing the transmittance (e.g., Perovich et al., 2002; Light et al., 2022). Observed differences in the timing and extent of melt ponds on multi-year ice (MYI) compared to first-year ice (FYI) (Webster et al., 2015; Polashenski et al., 2012; Buckley et al., 2020) suggest variability across ice types in the meltwater budget.

Thin meltwater layers under sea ice and in leads can form in calm conditions during the Arctic summer. The relatively fresh, warm water forms a stable layer on top of the saline ocean, separated by a sharp halocline. A recent review paper (Smith et al., 2023) summarizes observations of these layers and suggests that they are spatially and temporally heterogeneous but relatively common and persistent across many regions of the Arctic. In fact, these layers were noted as early as the Fram expedition and have been consistently observed since then (Nansen, 1902; Langleben, 1966; Ehn et al., 2011). Bottom melt rates may be reduced by the presence of strongly stratified fresher layers under the ice, which limit the transfer of heat from solar radiation (Skyllingstad et al., 2003; Hudson et al., 2013). The presence of under-ice meltwater can further support new sea ice growth during the melt season at the interface between the cold, saline ocean and fresher meltwater layer. These thin layers of ice formed at the interface are commonly called false bottoms (e.g., Eicken, 1994; Notz et al., 2003; Smith et al., 2022b; Salganik et al., 2023a).

The fate of freshwater in the sea ice system ultimately has broad impacts on the physics of the ocean and ice, ecosystems, and biogeochemistry (Smith et al., 2023). Our focus here is on the freshwater input from sea ice melt and snowmelt, which is just a small part of the Arctic Basin freshwater budget that includes any water source that is less saline than a reference seawater. On the basin scale, freshwater sources may include Pacific and Atlantic water inflows, precipitation, river runoff, ice sheet and glacier discharge, and sea ice melt, which can be redistributed between Arctic basins and also through sea ice growth, evaporation, and liquid and solid transport through ocean gateways (Lique et al., 2016; Solomon et al., 2021). Around 90 % of the sea ice export from the Arctic Ocean takes place in the Fram Strait, and the exported ice is an important source of freshwater to the North Atlantic (Haine et al., 2015). Once in the ocean, meltwater can strongly impact the thermohaline stratification and ocean circulation (Sévellec et al., 2017). Integration of meltwater into the upper ocean enhances stratification by reducing the density compared to underlying layers, while discrete near-surface meltwater layers create sharp density interfaces. Stratification due to sea ice melt and other freshwater sources plays a substantial role in the circulation and ventilation of the Arctic Ocean (Aagaard and Carmack, 1989). The strength of upper-ocean stratification impacts the vertical transport of heat and nutrients in the ocean (Schulz et al., 2024), the accumulation of solar heat (Hudson et al., 2013; Granskog et al., 2015), and communities and productivity (Ardyna and Arrigo, 2020; Gradinger et al., 2010), and it can create additional biological stresses (Chamberlain, 2023). The presence of a highly stratified meltwater layer, in particular, impacts gas exchange between the atmosphere and the ocean (e.g., Miller et al., 2019).

Recently, Perovich et al. (2021) synthesized data from the 1997–1998 Surface Heat Budget of the Arctic Ocean (SHEBA) experiment to compute a meltwater budget, addressing the following questions: how much meltwater is produced, and what are the relative contributions from different sources over time? This study computed a budget for multi-year ice from the sea ice perspective, where the fate of the meltwater within the ocean was not considered. This work raised the following question: how will sea ice and upper-ocean freshwater budgets change on and beneath different ice types in a changing Arctic Ocean? Here, we apply a similar approach to quantify a freshwater budget for the Multidisciplinary drifting Observatory for the Study of Arctic Climate (MOSAiC) expedition, which took place in summer 2020, observing a mix of first-year ice (FYI) and second-year ice (SYI). We examine both sources and sinks of meltwater. In contrast to the SHEBA experiment, meltwater sources are adjusted for ridge contributions using high-resolution observations of ridge fraction and melt, given their prevalence and more rapid melt than that of level ice (Salganik et al., 2023c), and we additionally estimate internal and oceanic sinks of relatively fresh meltwater.

2 Methods

This study combines various observations made during the MOSAiC melt season to quantify the freshwater budget. MOSAiC was a year-long drift experiment (October 2019–October 2020) on and around R/V *Polarstern* in the Central Arctic (Shupe et al., 2020; Nicolaus et al., 2022). The expedition was divided into multiple "legs", with some discontinuity between for logistical reasons; here we will focus on the melt season observations (Leg 4), which covered late June to the end of July. During that time, the ice floe adjacent to *Polarstern*, called the second Central Observatory (CO2), drifted from 82.0° N, 8.3° E to 78.8° N, 2.3° W. The floe comprised a mix of FYI and SYI. Autonomous instruments deployed earlier on the expedition were used to capture the onset of melt prior to the period of study; air temperatures above 0° C and snowmelt onset occurred in late May. The evolution of melt over the observed June–July period roughly progressed onwards with the first bottom melt at SYI observed on 6 June, the first under-ice meltwater layers at SYI on 16 June, the first melt ponds at SYI on 22 June, the first under-ice meltwater layers at FYI on 9 July, a large melt pond drainage event on 11–13 July, and ice floe break-up on 29 July. We use measurements from atmosphere, sea ice, and ocean observatories deployed across the floe to (1) quantify freshwater contributions from sea ice melt, snowmelt, and precipitation and (2) determine the distribution of that freshwater on the sea ice and in the ocean.

2.1 Sea ice and upper-ocean freshwater budget

Here we define a freshwater budget, where freshwater is defined in terms of the freshwater equivalent relative to a characteristic local ocean salinity. Notably, most of the sources and sinks are not fully fresh, and converting melt to a freshwater equivalent requires some knowledge of the sea ice salinity and density or solid fraction. During MOSAiC, the pre-melt bulk salinity of FYI and SYI was in the range of 2–5 $\mathrm{g\,kg^{-1}}$ (where FYI is typically saltier than SYI) (e.g., Angelopoulos et al., 2022; Salganik et al., 2023a). In some studies, a meltwater volume is alternatively used (e.g., Smith et al., 2022b) but is less appropriate for a budget where salinities of sources and sinks vary. For most terms, the meltwater volume can be converted to an equivalent freshwater volume by a factor of $1 - S/S_{\mathrm{ref}}$, where the ratio relates the salinity of the meltwater S to that of the reference seawater S_{ref}, taken as 34 $\mathrm{g\,kg^{-1}}$ here. The upper-ocean salinity was observed to evolve over time to closer to 32 $\mathrm{g\,kg^{-1}}$ (Fig. B1), while a reference salinity of 35.0 $\mathrm{g\,kg^{-1}}$ is used for freshwater transport monitoring by the Norwegian Polar Institute (2022) and 34.9 $\mathrm{g\,kg^{-1}}$ was used by Aagaard and Carmack (1989), which would result in an error of less than a couple percent in freshwater conversion for most of the relevant salinities used here. The ice salinity is taken as a fixed 3 $\mathrm{g\,kg^{-1}}$, which falls within the observational range for both ice types and is between the values of 2 ppt determined to be characteristic for Arctic summer sea ice in Vancoppenolle et al. (2009a) and the assumed value of 4 ppt in Aagaard and Carmack (1989). Fixed densities of 917 and 330 $\mathrm{kg\,m^{-3}}$ are used for sea ice and snow, respectively, following widely used parameterizations and are in general agreement with what was observed during the campaign (Alexandrov et al., 2010; Salganik et al., 2024).

During the melt season, possible sources of freshwater include snowmelt (M_{snow}), surface sea ice melt ($M_{\mathrm{i,surf}}$), bottom sea ice melt ($M_{\mathrm{i,bottom}}$), lateral sea ice melt ($M_{\mathrm{i,lat}}$), precipitation (rain; P), and condensation. Condensation and evaporation are both vanishingly small, as estimated by effectively no net change in the cumulative latent heat flux measured at MOSAiC during the period of study (Cox et al., 2023). The snow, surface sea ice melt, and precipitation over the ice all provide freshwater sources at the surface of the ice, while bottom and lateral ice melt and precipitation in leads provide freshwater directly to the ocean.

Sinks of meltwater include storage in melt ponds (V_{mp}), under-ice meltwater layers (V_{ui}), lead meltwater layers (V_{lead}), entrainment into the upper ocean (V_{uo}), and internal storage in the ice and ridges (V_{internal}). Under-ice meltwater layers can be assumed to generally be a result of vertical drainage, while lead meltwater layers are presumed to be primarily a result of lateral or horizontal drainage. Freshwater is also likely stored in the ice during the melt season through the melt and drainage process by the replacement of brine and by re-freezing in ridge keels (V_{internal}).

The budget is then defined over the sea ice and upper ocean:

$$M_{\mathrm{snow}} + M_{\mathrm{i,surf}} + M_{\mathrm{i,bottom}} + M_{\mathrm{i,lat}} + P = V_{\mathrm{mp}} + V_{\mathrm{ui}} + V_{\mathrm{lead}} + V_{\mathrm{uo}} + V_{\mathrm{internal}}, \quad (1)$$

where the calculation of terms is described in the subsections that follow. Here, the budget terms represent a cumulative volume relevant to the beginning of the melt season (or the start of available data). Many source terms are initially calculated as a rate which is then summed to calculate a cumulative value, while many sink terms are calculated directly as a volume. We assume a one-dimensional (1D) budget, where volumes are scaled by the area ($\mathrm{m^3\,m^{-2}}$), simplifying to a unit of length (m). The area the budget is calculated over is generally the MOSAiC CO2 floe (Fig. 1), plus an additional 100 m border to include the fraction deposited into adjacent leads (Fig. A1). Thus, all terms are scaled by the open-water or ice-covered fraction. This represents a difference from the budget calculated in Perovich et al. (2021), which calculated a 1D budget of ice-covered area only.

The open-water fraction is determined by thresholding aerial orthomosaics of the floe (Fuchs, 2023; Neckel et al., 2023). The estimate is made over the area of the floe plus a 100 m ring (shaded red areas in Fig. A1). Images to make such estimates are only available for three dates (30 June,

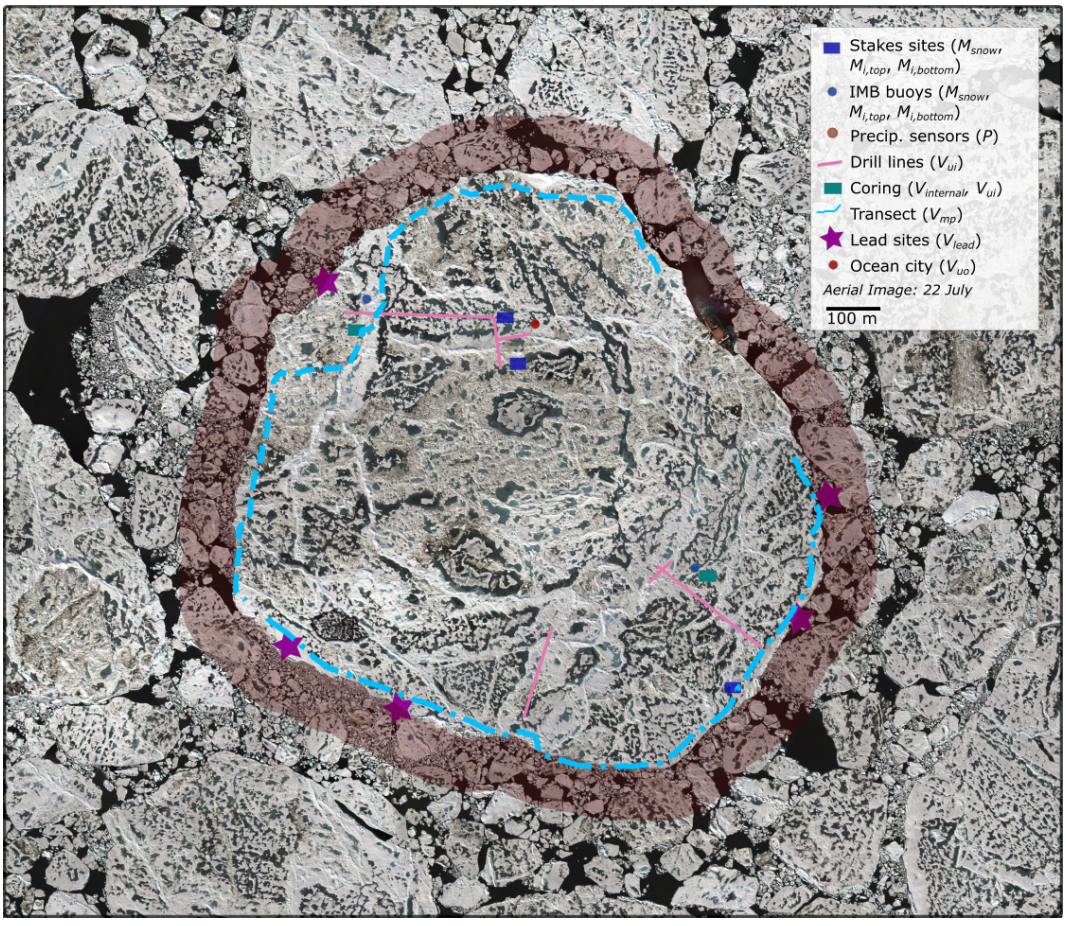

Figure 1. Map of locations of measurements used in budgets. The shaded red ring denotes the 100 m border over which the open water (OW) fraction is calculated. The full mass balance transect is shown as a blue line, dashed portions denote SYI, and dash-dotted portions denote FYI. Note that only the locations of ice mass balance (IMB) buoys on the CO2 floe are shown. See Nicolaus et al. (2022) for a full map of the floe drift.

17 July, and 22 July) so a linear interpolation is used for dates between to enable continuous budget calculations. Open-water fraction estimates on 30 June, 17 July, and 22 July are 3.3 %, 9.6 %, and 5.2 % (Fig. A1), respectively. Comparisons with satellite product estimates of sea ice concentration from Bootstrap (Comiso, 2000) and NASA Team (DiGirolamo et al., 2022) methods at the MOSAiC location over the same time period show that these values are within the range of observational estimates, which have a standard uncertainty of around 20 % for summertime retrievals, corresponding to an error of a couple percent for the airborne open-water fraction estimates.

The floe (Fig. 1) contains a combination of FYI and SYI (Guo et al., 2023; Kortum et al., 2024). We assess differences in budget terms over known FYI and SYI portions of the floe, where possible, including the sources from melt and the melt pond sink term (V_{mp}). However, it is not possible to complete a full budget for both due to insufficient data to address all terms for the separate ice types. Additionally, as the upper ocean interacts with both FYI and SYI, attempting to separate the budget of these ice types is not representative of the reality of such a composite floe.

2.2 Freshwater sources

2.2.1 Snowmelt and ice melt (M_{snow}, $M_{i,surf}$, $M_{i,bottom}$)

Snowmelt and sea ice melt are estimated from a combination of two methods which use the approach of measuring the evolution of interfaces: sea ice mass balance stakes (hereafter stakes) and ice mass balance (IMB) buoys. Estimates of snowmelt and sea ice melt terms from the two methods are compared, and the values are taken as an average, as shown in Fig. 3.

During the observational period, arrays of stakes were deployed on three areas of the floe to provide a representative sample (Raphael et al., 2022). For example, 38 % of the stakes were in melt ponds at some point with a peak melt pond fraction of 23 %, which generally agrees with the satel-

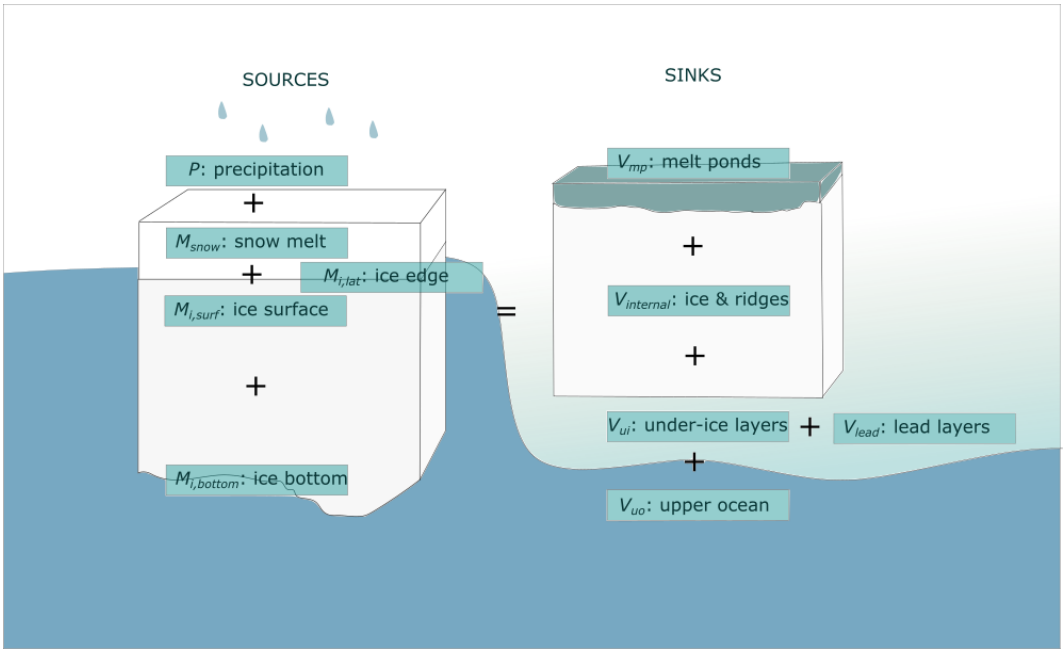

Figure 2. Schematic of key terms of the freshwater budget, with sources on the left and sinks on the right. The source term "ice bottom" includes an adjustment for the ridge fractional coverage. The dark-blue background represents the shifting depth of the interface of saltwater with fresher water.

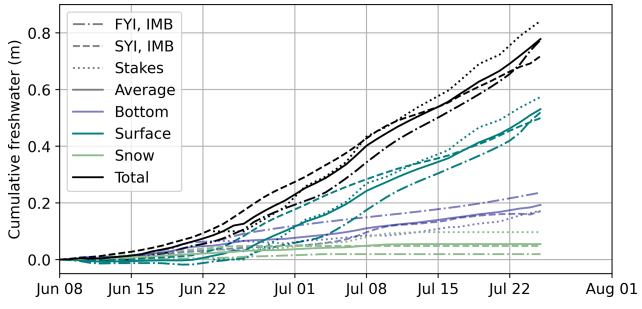

Figure 3. Estimation of sea ice melt and snowmelt freshwater source terms from stakes (dotted lines) and IMB buoys. IMB buoys are separated into FYI (dash-dotted lines) and SYI (dashed lines). The average across all methods (solid lines) is used as the best estimate of each term, including bottom melt (navy), surface melt (teal), and snowmelt (green), in subsequent analysis.

lite estimates from Niehaus et al. (2023) and Webster et al. (2022). Terms are averaged across all stakes to provide estimates from 26 June onwards. More details can be found in Raphael et al. (2024). As the installation of stakes in late June missed the initial melt onset, the melt of snow and ice prior to 26 June was estimated using an IMB buoy at a site known as L2, 0.7° east of the floe on 1 July, which had representative ice and snow thickness values (Perovich et al., 2023; Raphael et al., 2024). The SIMB3 buoy suggested that all change in surface elevation prior to 26 June was due to snowmelt. A comparison of meltwater production from snowmelt and ice melt between L2 IMB and stakes from 26 June–29 July (not shown) is quite consistent, suggesting that this provides a robust estimate of meltwater production for level ice and that the L2 observations between melt onset and 26 June are likely representative of the CO2 floe.

A total of 18 IMB buoys were operational during Leg 4 of MOSAiC on the CO2 and surrounding floes (Rabe et al., 2024). Of these, 12 were deployed in SYI, 3 were deployed in FYI, and 3 were undefined or other, with maximum ice thicknesses ranging 1.55–5.94 m and maximum snow thicknesses ranging 0.13–0.62 m (with the largest for either being an outlier from a buoy in a first-year ridge). For the purpose of snowmelt and ice melt calculations, the dataset was restricted to IMBs that are on a known ice type that covered the entire period through 25 July. This left 5 IMB buoys in SYI, with maximum ice thicknesses of 1.71–2.92 m and maximum snow thicknesses of 0.15–0.36 m, and 3 IMB buoys in FYI, with maximum ice thicknesses of 1.55–1.86 m and maximum snow thicknesses of 0.14–0.20 m. Each set includes 1 buoy in the MOSAiC CO2.

Recent work has shown that the melt of ridge keels provides a larger and more rapid input of meltwater compared to level ice (Salganik et al., 2023c). Most mass balance measurements used in these estimates were made over relatively level ice (avoiding ridge keels). Furthermore, since the melt of ridge keels is highly spatially heterogeneous, it is not well captured by point measurements from stakes or IMBs. We make an adjustment to the bottom ice melt estimate based on the ridge (keel) fraction, A_{ridge}, and the ratio of ridge keel

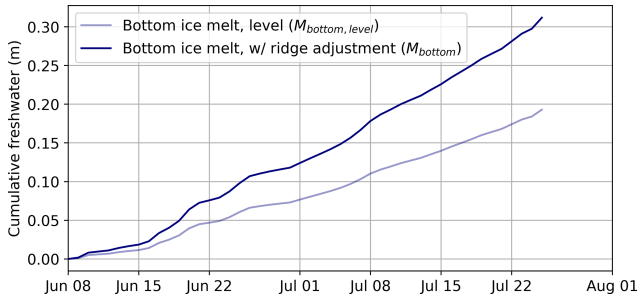

Figure 4. Impact of ridge keel coverage adjustment on the calculation of cumulative bottom ice melt freshwater production. The initial calculation using mass balance buoy and stakes only, from relatively level ice ($M_{\text{bottom,level}}$), is shown in lighter transparent blue, and the total estimate of bottom ice meltwater with the keel melt adjustment (M_{bottom}) is in navy.

melt to level ice melt rate, $R_{\text{ridge/level}}$:

$$M_{\text{bottom}} = (M_{\text{bottom,level}} \cdot (1 - A_{\text{ridge}})) + (R_{\text{ridge/level}} \cdot M_{\text{bottom,level}} \cdot A_{\text{ridge}}), \quad (2)$$

where $R_{\text{ridge/level}}$ is assumed as a constant 3.8 based on results from Salganik et al. (2023c) using repeated multibeam sonar surveys. A_{ridge} is estimated by correcting the ridge sail fraction with a sail-to-keel-width ratio. The sail fraction is estimated as 8 % using the using airborne laser scanning (ALS) data from July with a 0.6 m freeboard threshold (Hutter et al., 2021). The sail-to-keel ratio was estimated as 2.7 using colocated ALS and remotely operated underwater vehicle sonar data with the same freeboard threshold (Hutter et al., 2021; Salganik et al., 2023c). This ratio is slightly lower than previously estimated ratios of Arctic FYI ridges of 3–7 (Strub-Klein and Sudom, 2012) and 4.1 (Guzenko et al., 2023). This suggests a keel areal fraction A_{ridge} of 22 ± 4 %. This is in agreement with pan-Arctic estimates of 12 %–20 %, assuming a typical keel width of 36 m (see Strub-Klein and Sudom, 2012) and an average ridge sail spacing of 250–300 m (e.g., Mchedlishvili et al., 2023; Zhang et al., 2024). The impact of this adjustment on bottom melt estimates is shown in Fig. 4.

2.2.2 Lateral ice melt ($M_{\text{i,lat}}$)

As direct measurements of lateral melt were not made during MOSAiC, we provide an estimate of the approximate contribution from lateral melt using the change in floe size estimated from orthomosaics (Neckel et al., 2023). Estimates of the floe size were available for three dates: 30 June, 17 July, and 22 July. Approximate lateral melt contribution between these dates was estimated by multiplying the change in floe area by the average ice thickness from mass balance surveys (Itkin et al., 2023), in order to get the change in floe volume, and scaling by the initial area. We note that change in floe size may be a result of both thermodynamic loss (lateral melt) and dynamic loss (breaking of the floe); here we assume that all loss in area is due to thermodynamic processes. The error in this rate estimate is likely large, but it contributes a small fraction to the total freshwater estimate.

2.2.3 Precipitation (P)

The liquid-phase precipitation (rain) estimates were made in two ways. Firstly, an optical measurement of precipitation was made by a present weather detector (PWD) installed above the bridge of the ship (Kyrouac and Holdridge, 2019). This sensor has been shown to be a superior measure of snowfall in the winter compared to other precipitation gauges at MOSAiC, as it minimized the impacts of blowing snow (Matrosov et al., 2022), although it is not clear how this result translates to liquid-phase precipitation in summer. Additionally, since it was installed on board the vessel, it was operated nearly continuously, providing an uninterrupted dataset. The second approach was to identify periods of liquid-phase precipitation using a multi-sensor approach based on cloud radar and other instruments operated on board *Polarstern* (e.g., Shupe, 2007, 2022) and then to apply an appropriate radar-reflectivity-based power-law retrieval (e.g., Chandra et al., 2015). The radar reflectivity measurements came from a Ka-band ARM Zenith Radar (KAZR) operated from *Polarstern*, with precipitation retrievals being applied to measurements at a height of 190 m above the surface, which is the lowest range gate from the radar data that avoids any near-surface influences. Precipitation is assumed to be consistent below that height.

Here, we use an average of the two methods (solid gray line in Fig. 5) to quantify the rate and cumulative accumulation of in situ precipitation. The uncertainties are quantified as the average of minimum and maximum uncertainty values from the radar and PWD methods. Uncertainties in the radar-based approach may come from three primary sources. Firstly, the calibration of the radar reflectivity is assumed to contribute uncertainty up to 3 dBZ. The second source of uncertainty is the inversion of radar measurements to retrieve a precipitation rate, and we include here the highest and lowest values retrieved from approaches in the literature. The third source of uncertainty is associated with potential misidentification of conditions (rain vs. drizzle), which is ignored here as most conditions were representative of rain. The upper bound on radar-based precipitation is thus estimated as the retrieval method with the highest estimated accumulation with a reflectivity that was measured plus 3 dB. The lower bound on radar-based precipitation is estimated as the retrieval method with the lowest estimated accumulation using a reflectivity that was 3 dB less than what was measured (where both are shown as dotted blue lines). The uncertainties associated with the PWD have been less well quantified. Based on comparisons given in the literature, we approximate the uncertainty as 30 %, so a ± 30 % uncertainty is applied to the observations (dotted red lines). PWD gives a higher overall estimate than the radar method, but the es-

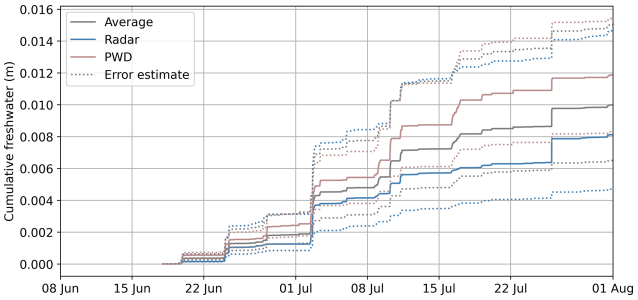

Figure 5. Cumulative freshwater precipitation in meters from late June to the end of July 2020. Estimates from radar (pale blue) and PWD (pale red) are averaged together (gray) to give a best estimate of precipitation for use as P. The error estimates given minimum and maximum values (dotted lines) from the two methods are averaged together to give the best estimate of total observational uncertainty.

timated average 0.01 m rain accumulation falls within the plausible range from both methods.

2.3 Freshwater sinks

2.3.1 Melt ponds (V_{mp})

Melt pond depths and fraction are estimated using the modified Magnaprobe estimates along the Leg 4 transect (Itkin et al., 2021; Webster et al., 2022), excluding any special surveys or albedo lines. Estimates include both the depth of standard melt ponds and those defined as subnivean ponds. We include results for the separation of transect data into SYI and FYI, where delineation of the floe into ice types was determined by observers on the floe (SYI is denoted by the dotted blue line in Fig. 1, and FYI is denoted by the dashed line; Webster et al., 2022). Conversion to freshwater equivalent assumes that melt ponds have a practical salinity of 1.1 as an average of measurements made in July (Lange et al., 2022), which was generally consistent with the full observed range of 0.5–2 across ponds and ice types (Oppelt and Linhardt, 2023).

2.3.2 Meltwater layers under ice (V_{ui})

Freshwater in under-ice meltwater layers is estimated primarily using layer thicknesses from all of the 18 IMB buoys operable during the melt season (see description of buoys in Sect. 2.2.1). While the IMB buoys captured a range of sea ice types, we note that these may constitute an unrepresentative sample. The top and bottom extent of the meltwater layers, when present, are determined based on the location of the ice–meltwater interface and the meltwater–ocean interface using the rate of change after heating cycles and ambient temperature, respectively (Jackson et al., 2013). As the thermistor strings on the buoys have 2 cm spacing in sensors, an accuracy of 2 cm can be assumed. IMB buoys provide estimates of temperature and thus interfaces every 6 h, which we average to calculate a daily value. We calculate the layer thickness as an average across all instruments where a layer was observed on that day.

Estimates of under-ice meltwater layer thickness from IMB buoys are compared in Fig. 6 with those measured along drill lines (orange lines in Fig. 1) by deployment of a YSI Professional Plus probe measuring temperature and conductivity (Smith et al., 2022b) and with those made at the coring site (teal box in Fig. 1; Salganik et al., 2023a). The coring site estimates are consistent with, but smoother than, the estimates from IMB buoys, while the YSI estimates seem to provide a "lower bound" from a different region of the floe (SYI). We note that a layer of under-ice meltwater was also observed at the Ocean City hole using a microstructure profiler from 28 June to 13 July (Smith et al., 2023; Schulz et al., 2022), but those observations are not included here due to suspected biases associated with artificially accelerated meltwater drainage and the location in SYI.

The conversion from meltwater layer thickness (Fig. 6) to equivalent freshwater thickness accounts for the salinity of the layer, which is not fully fresh, and the spatial coverage under the ice. Here we assume a constant salinity of 8 based on an approximate temporal best fit of all salinity estimates included in Smith et al. (2022b). A constant fractional coverage of 21 % is assumed (Salganik et al., 2023a), as information is too sparse to justify more temporal variability in coverage, and this value is approximately consistent with the estimates in Smith et al. (2022b). This is lower than the fractional estimate based on the fraction of IMBs in which meltwater layer was observed (8 out of 18; 44 %), which may be biased high due to the fact that IMB installation typically occurs in areas of undeformed ice far from floe edges, which are more prone to under-ice meltwater layer formation.

2.3.3 Meltwater layers in leads (V_{lead})

Freshwater equivalent estimates for lead meltwater layers are approximated as the average of all measurements available from profiling by a YSI Professional Plus probe (as used for under-ice measurements; Smith et al., 2021a) or fishing rod CTD for a given day (Karam et al., 2023) (Fig. 6). Here, profiles were generally made from the lead edge or a kayak, to minimize disruption of the surface stratification. Calculation of the equivalent freshwater layer thickness results in estimates that range from 72 %–150 % of the depth of the maximum density change, and equivalent freshwater estimates are more consistent between the two instruments than estimates of meltwater layer thickness (YSI and fishing rod CTD). Lead meltwater layer estimates are scaled by the open-water fraction (Fig. A1), whereas all sea-ice-based estimates are scaled by the ice-covered fraction.

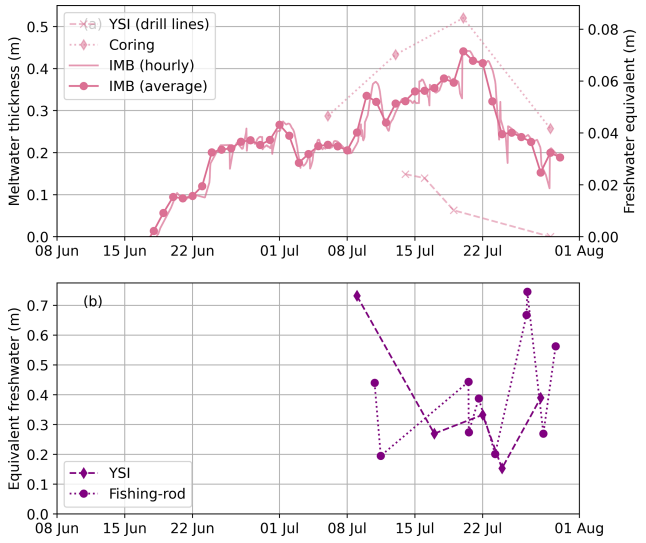

Figure 6. (a) Comparison of estimates of under-ice meltwater layer thickness (left axis) and equivalent freshwater thickness (right axis; V_{ui}) from different observational methods, prior to scaling for coverage. Estimates from drill lines (dashed) and the FYI coring site (dotted) are shown for comparison to the average layer thickness from IMBs (solid line). **(b)** Estimates of freshwater layer thickness in leads, V_{lead} (prior to scaling for open water fractional coverage), from YSI (dashed line, diamonds) and fishing rod CTD (dotted line, circles).

2.3.4 Upper ocean (V_{uo})

While sub-daily estimates of upper-ocean temperature and salinity are available for the duration of the period (Schulz et al., 2024), estimates of freshwater input to the upper ocean are complicated by the drifting nature of the experiment. Notably, in this period, the MOSAiC floe drifted into a regime with lower ambient seawater salinity and higher river water fractions (see Schulz et al., 2024) (Appendix B), which dramatically increased the apparent "freshwater content" in a manner that is not entirely related to local inputs from sea ice. As a result, we do not directly estimate entrainment of freshwater into the upper ocean and rather treat this term as a residual.

2.3.5 Internal storage ($V_{internal}$)

Sea ice ejects salt to the upper ocean during both growth and melt, directly impacting the salt content of the surrounding seawater through desalination processes. These include gravity drainage and flushing during the melting season. Gravity drainage is the exchange of the dense brine in the ice with seawater by convective overturning triggered by a heat-induced increase in ice permeability. Flushing is the replacement of the salty brine in the ice with surface meltwater percolating through the ice (Notz and Worster, 2009). In relative terms, both processes reduce the freshwater equivalent by releasing a salt mass Δm_{salt} from the ice into the ocean and thus form a sink term in the freshwater budget that we consider with $V_{internal}$. Following the scheme to start from the surface meltwater, $V_{internal}$ is derived here from the volume difference of the freshwater equivalent of the surface meltwater ($V_{MW,surf} = M_{snow} + M_{i,surf} - V_{mp}$) before draining through the ice ($V_{MW,equ}(in)$) and after ($V_{MW,equ}(out)$):

$$V_{internal} = V_{MW,equ}(in) - V_{MW,equ}(out). \quad (3)$$

The freshwater equivalent of the surface meltwater before draining into the ice was obtained by scaling the available surface meltwater $V_{MW,surf}$ using

$$V_{MW,equ}(in) = V_{MW,surf} \cdot \left(1 - \frac{1.1\,g\,kg^{-1}}{S_{ref}}\right), \quad (4)$$

for which we assume a constant salinity of $1.1\,g\,kg^{-1}$ of the surface meltwater (Lange et al., 2022) and the previously defined reference salinity $S_{ref} = 34\,g\,kg^{-1}$.

After draining through the ice, the volume of meltwater remains constant, i.e., isochoric, but the salt content changes; thus the freshwater equivalent changes to

$$V_{MW,equ}(out) = V_{MW,surf} \cdot \left(1 - \frac{S_{MW}}{S_{ref}}\right) \quad (5)$$

with the increased salinity of the drained meltwater:

$$S_{MV} = \frac{\Delta m_{salt}}{(\Delta m_{salt} \cdot 1000 + m_{MW,surf})}. \quad (6)$$

The generalization across all desalination processes was made to be able to derive a time series of $V_{internal}$ both with measurement data, combining the observed total loss of salt in ice cores Δm_{salt} with surface meltwater, and with simulations, which fully resolve all individual desalination processes using the multiphase thermodynamic single-column model Semi-Adaptive Multi-phase Sea-Ice Model (SAM-SIM; Griewank and Notz, 2013). The model was initialized and run separately with ice core data from FYI and SYI from early May (Oggier et al., 2023a, b) and then forced with a set of boundary conditions. Boundary conditions used a merged time series of observed atmospheric boundary fluxes (Pirazzini et al., 2022), ERA-5 data as gap fillers (Hersbach et al., 2017), a rather small constant oceanic heat flux of $1\,W\,m^{-2}$, and an initialized snow thickness of about 22 cm based on observations. Changes in salinity of the underlying ocean water due to the formation of the meltwater layer are not considered in the model. Given these forcings, the model simulated ice evolution similar to the observed ice core measurements. Bulk brine volume estimates from IMB buoy temperature observations are very similar to those from coring observations in magnitude and temporal evolution on both FYI and SYI (Fig. C2), giving confidence to the applied estimates.

Meltwater can also re-freeze in ridge keels during summer (e.g., Salganik et al., 2023b), which may provide a transient

sink in opposition to the source from accelerated ridge keel melt. We do not make explicit estimates of it here, as reliable pre-melt-season salinities are not available. However, we expect the term to be relatively small, as the keel macroporosity in June was already very low (4 %–6 % for a ridge on the same floe), suggesting low meltwater mass fraction (Salganik et al., 2023b).

3 Results

3.1 Freshwater sources

Estimates of sea ice and snow source terms from methods and ice types are compared in Fig. 3. Initially, there is approximately 2–3 times more surface and snowmelt on SYI than FYI but around 2 times more bottom melt on FYI than on SYI. By the end of the observation period (late July), the cumulative freshwater produced on both ice types approximately converges, with the larger bottom melt of FYI (40 % greater; 6 cm) mostly compensating for the larger snowmelt on SYI (2.5 times greater; 3 cm). The estimates from stakes on both ice types sit mostly between the estimates for FYI and SYI from IMB buoys, though with a somewhat larger freshwater contribution from snowmelt and surface melt estimated by the end of the period. In general, the relative ranking of terms is consistent across methods and ice types.

The bottom melt on relatively level ice (solid blue line in Fig. 3) is adjusted for the higher melt rate observed on ridge keels in Fig. 4, following Eq. (2). Ridge keel melt is estimated to contribute cumulatively around 0.12 m of freshwater by the end of the period, increasing cumulative bottom melt estimates by over one-third (navy line in Fig. 4).

All source budget terms are summarized in Fig. 7. The rate of freshwater input from all terms appears quite episodic, as dictated by atmospheric and ocean forcing. The contribution from surface ice melt is initially close to zero, as solar energy is likely focused on snowmelt, and some buoys observed a re-freezing of melt ponds. The surface and bottom sea ice melt ($M_{\mathrm{i,surf}}$, $M_{\mathrm{i,bottom}}$) generally accelerate over the course of the observation period. In contrast, the contribution from snowmelt (M_{snow}) ceases on 13 July, when nearly all snow had melted on level ice (Macfarlane et al., 2023; Webster et al., 2022). Lateral melt estimates ($M_{\mathrm{i,lat}}$) suggest that it is a low fractional contribution through the period (less than 5 % of the total). The contribution from precipitation is episodic, with a total cumulative contribution barely over 1 cm. The largest overall contribution to the cumulative freshwater is from surface sea ice melt.

Both precipitation-related source terms (M_{snow} and P) in total contribute less than 7 % of freshwater to the cumulative total by the end of the period. Given the uncertainty in both initial snow thickness and precipitation of up to 50 % (Itkin et al., 2023; Fig. 5), we estimate this could range from 4 %–10 %. Figure 8 compares the relative contributions from these

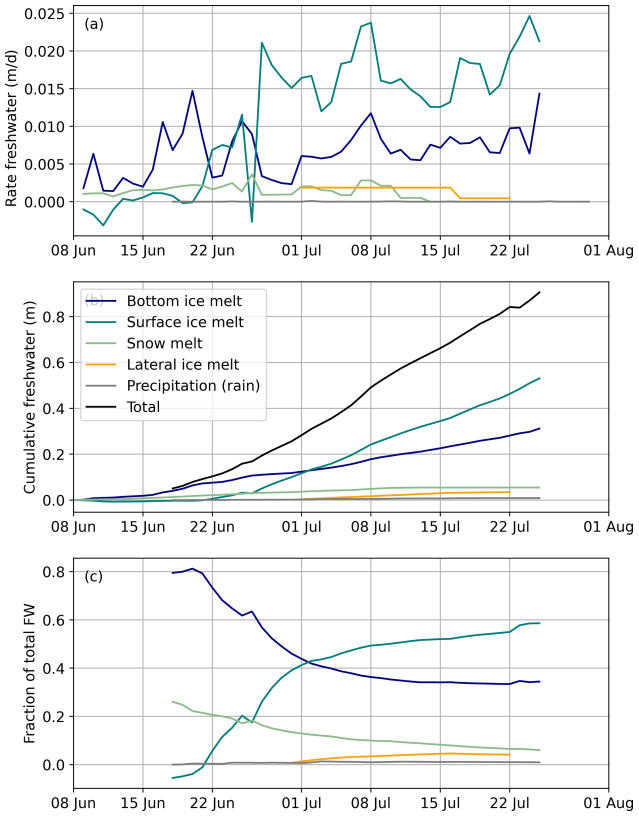

Figure 7. Summary of freshwater production (freshwater equivalent) from early June to late July 2020. **(a)** Rate of freshwater production from bottom ice melt (navy), surface ice melt (teal), snowmelt (green), lateral melt (yellow), and precipitation (gray). **(b)** Cumulative freshwater from early June to late July, including the total of all terms (black). **(c)** The fraction of total freshwater (FW) contributed by each term.

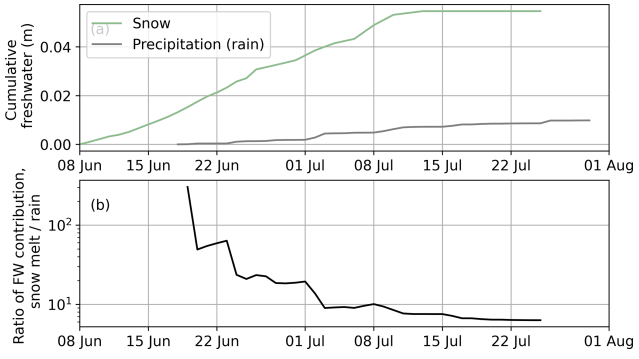

Figure 8. Comparison **(a)** and relative contribution **(b)** from stored precipitation (snow; green) and in situ precipitation (gray).

terms. The ratio is very high initially (> 100), as snowmelt is rapid and little rain has yet been recorded. By the end of the observation period, stored precipitation (snow) contributes around 6 times as much to the freshwater budget as in situ precipitation (rain). The relative fraction is likely to continue

to decrease past the period of this time series, as precipitation may continue in August but the snow has virtually all melted.

3.2 Freshwater sinks

Figure 9b shows that storage in melt ponds is notably higher on SYI (dashed line) compared to FYI (dash-dotted line). Equivalent freshwater storage is over twice as large on SYI at times. The temporal evolution on FYI is less extreme compared to that on SYI through the middle of the observation period, likely owing to the earlier formation of lateral drainage channels on FYI (Webster et al., 2022). However, the temporal evolution is largely similar between the ice types, suggesting that the drivers of sources (meltwater input) and loss via drainage are not independent. Some of the temporal variability on the FYI portion of the transect from 20 July onward could be biased by necessary relocation of the transect as melt ponds melted completely through (Webster et al., 2022). The substantial decrease from 10–14 July on the SYI was associated with a large pond drainage event that was visible from the floe and in aerial imagery and resulted in a large reduction in both melt pond fraction and depths (Webster et al., 2022) and an increase in ice freeboard (e.g., Salganik et al., 2023c). The average melt pond freshwater storage along the full transect (solid line) is used for the comparison of sink terms in subsequent analysis.

We note here that the estimates of freshwater in melt ponds during MOSAiC, as quantified from transect data, may be biased low due to the location at the periphery of the ice floe (Fig. 1), where lateral drainage is greater. Specifically, estimates of freshwater equivalent from bathymetric reconstructions of orthomosaics suggest approximately twice as much freshwater stored in melt ponds in the first half of the period (30 June and 7 July) compared to transect observations (Fuchs et al., 2024). Further investigation into these differences suggests that this is likely mainly due to differences in observed areas instead of methodological differences (Fuchs et al., 2024). The orthomosaic estimates are not used here due to sparse temporal coverage, and the reader is referred to Fuchs et al. (2024) for more details on these observations.

Internal storage of freshwater due to desalinization based on observational (coring) data and modeling is shown in Fig. 10. The fully resolving model indicates a higher V_{internal} for both ice types over the entire summer melt and indicates two main desalination periods: the first in late May through warming of the ice interior, during a period when there is a gap in coring and other observational datasets, and a second period starting mid-July. The observations additionally capture the rapid increase in FYI storage in mid-July. While both ice types showed the same amount of total surface melt over the observational period (Fig. 3), FYI typically desalinates more and stores more freshwater. We thus use the estimate from FYI cores (dark-brown dash-dotted line in Fig. 10b) as the time series of internal freshwater storage V_{internal} in subsequent comparisons, providing a likely upper bound on the

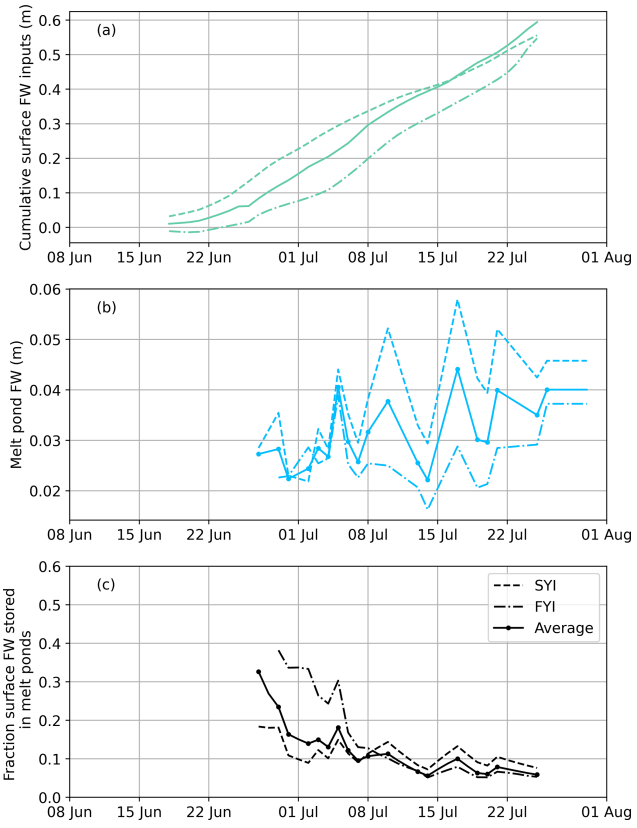

Figure 9. (a) Cumulative surface freshwater input on SYI (dashed) and FYI (dash-dotted) from combined surface ice melt, snowmelt, and precipitation. **(b)** Melt pond equivalent freshwater thickness for SYI and FYI. The solid line shows the equivalent thickness for the full transect on each date, while the dashed and dash-dotted lines show equivalent thicknesses over just the SYI and FYI sections, respectively (see Fig. 1). **(c)** The ratio of freshwater in melt ponds to the freshwater input **(b/a)** provides an estimate of the melt pond fractional storage. Following the initial peak in storage on 27 June, the storage **(c)** gradually decreases throughout July largely due to the steady increase in input from surface meltwater **(a)** which is not matched by a comparable increase in equivalent pond volume **(b)**.

term. Sensitivity of these terms is approximated using runs where forcing terms are given the following ranges: ocean heat flux from 0.5–10 W m^{-2}, reference salinity S_{ref} from 32–34.9 g kg^{-1} (Schulz et al., 2024; Norwegian Polar Institute, 2022), and meltwater salinity S_{mw} from 0.6–1.9 g kg^{-1} based on the range of observed melt pond salinities (Smith et al., 2022b; Lange et al., 2022). The range of all runs for coring and model calculations is shown as shading in Fig. 10 and suggests errors from around 5 %–100 %. For the FYI core estimates used in subsequent calculations, this represents a 9 % range. We do not explore in detail the relative sensitivity of the estimated meltwater value to the input terms, but results suggest the greatest impact is that of the meltwater salinities.

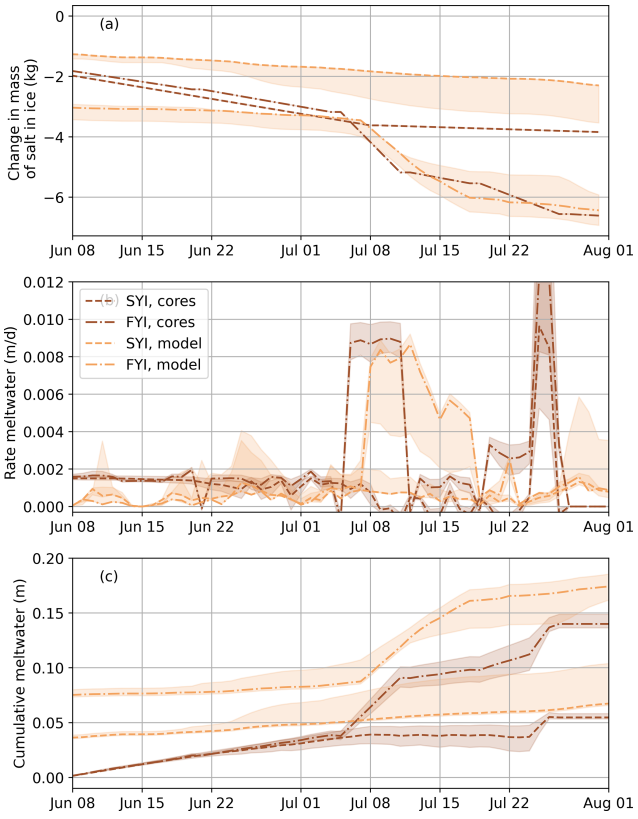

Figure 10. Estimates of salt internally in ice and contribution to freshwater sink. **(a)** The change in mass of salt in ice, relative to the start of the melt season, is used to calculate the **(b)** rate and **(c)** cumulative freshwater stored internally in the sea ice (V_{internal}). Estimates are shown based on coring observations (dark brown) and a 1D model (light brown) for SYI (dashed) and FYI (dot-dashed).

Quantified freshwater sink terms both on the ice and in the upper ocean are combined in Fig. 11. Melt ponds and under-ice meltwater layers were observed from near the beginning of the record, with lead meltwater layers only first being observed on 8 July. Thus, under-ice layers and melt ponds are the dominant sink in early July. Under-ice meltwater layers constitute a significant fraction of the observed sinks, with melt ponds and leads representing approximately the same volume from the middle to the end of July. In mid-July, internal storage in the sea ice becomes the dominant sink, with over 0.10 m equivalent freshwater storage by the end of the observation period. The total freshwater equivalent stored in the quantified sinks (black line in Fig. 11) peaks at 0.25 m in late July.

3.3 Sources vs. sinks

By comparing the melt pond term with the surface sources, we can understand the efficiency of melt ponds as sinks. Sources for melt ponds include snowmelt, sea ice melt, and precipitation, which can be determined from the results in

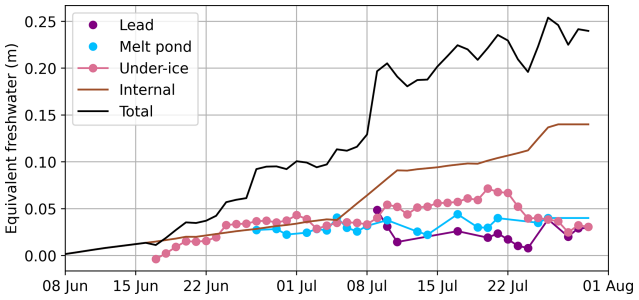

Figure 11. Summary of meltwater sinks (freshwater equivalent) from mid-June to late July. The total (black) includes estimated freshwater in leads (purple), melt ponds (cyan), under-ice (pink), and internal in the ice (brown).

Fig. 7 to calculate the cumulative surface freshwater input (Fig. 9a). Dividing this by the melt pond volume, V_{mp}, following Perovich et al. (2021), gives an estimate for the fractional storage of surface freshwater in melt ponds in Fig. 7c. During their initial formation, melt ponds are an efficient sink for surface meltwater, with over 45 % estimated on 27 June. This rapidly decreases with a decrease in freshwater in melt ponds in late June, and fractional storage remains below 20 % throughout July.

Figure 9c also shows differences in the relative melt pond storage of ice types. Initially, FYI stores more surface meltwater than SYI, but SYI stores a higher relative fraction after 7 July. As both surface meltwater inputs and melt pond freshwater volume are higher throughout the summer on FYI, this temporal shift largely results from a decline in the rate of surface freshwater production on FYI over time.

Comparing the total quantified freshwater sinks with estimates of sources provides insight into the full freshwater budget and the residual that is deposited into the ocean. By the end of the observation period, 0.68 m or 75 % of the estimated sources (Fig. 7) are unaccounted for by observed sinks (Fig. 11). This suggests that a majority of local freshwater from sea ice melt and snowmelt is ultimately entrained into the upper ocean. We can use this to make some indirect inferences about the residence time of freshwater within the various sinks. While the magnitude of freshwater within lead, melt pond, and under-ice sinks does not significantly grow over time, freshwater sources provide relatively consistent new inputs. It is thus likely that most of the freshwater that ends up in the upper ocean passes through one of these other sinks first. In other words, initial increases in the under-ice freshwater sink suggest that the flux of freshwater from sources is outpacing the mixing into the upper ocean, while the decrease later in the observation period suggests that the mixing is outpacing new inputs.

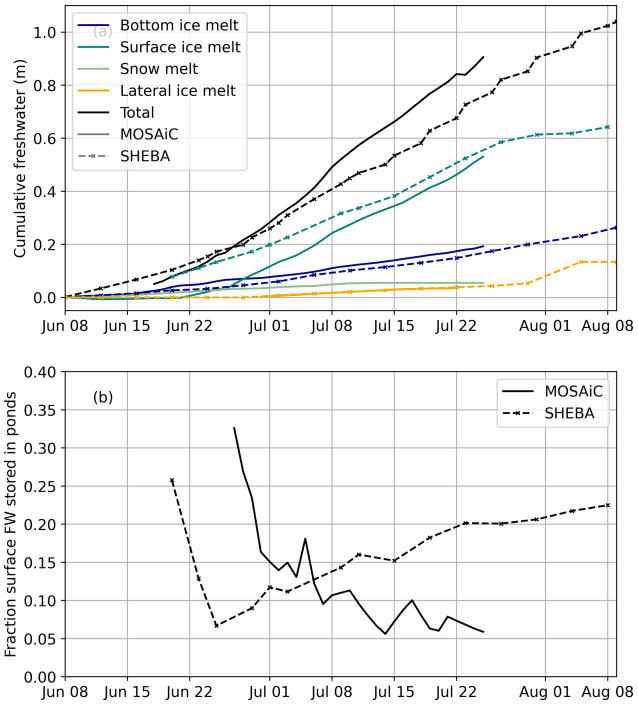

Figure 12. Comparison of meltwater budget terms from MOSAiC (solid) and SHEBA (dashed). **(a)** Cumulative meltwater source terms, noting that snow is not shown for SHEBA, and **(b)** fractional melt pond storage.

4 Discussion

4.1 Comparison with prior observations: SHEBA

Perovich et al. (2021) provided one of the first comprehensive budgets of meltwater in Arctic sea ice using observations from the 1997–1998 SHEBA datasets. Notable differences between MOSAiC and SHEBA include that sea ice during MOSAiC was a mix of FYI and SYI, while SHEBA occurred on dominantly MYI. Additionally, MOSAiC was in the Central Arctic, approaching the Fram Strait by the time of the melt season, while SHEBA occurred in the Beaufort Sea. Some changes in conditions can also be expected as a result of the 22 years separating the expeditions. More extensive quantification of thin meltwater layers in the ocean on MOSAiC (e.g., Smith et al., 2022b, 2023) also allowed the calculation of sinks.

Figure 12a compares the cumulative freshwater inputs from major sea ice and snow sources. The total cumulative input is remarkably similar between the two by the end of the comparison period, despite the differences in conditions. Notably, the contribution from bottom melt closely tracks between the two sets of observations, despite the significant adjustment for contribution from ridges on MOSAiC. The multi-year ridges during SHEBA were smoother and so produced less meltwater than typical FYI ridges, with only 1.6 times more bottom melt at ridge keels (Perovich et al., 2003). The surface melt was a larger fraction of melt on both campaigns but accelerated more rapidly earlier in the melt season during SHEBA. The lateral melt is a minor fraction ($\sim 5\,\%$) on both campaigns by the end of July. In both, the contribution from summer precipitation is small compared to other terms and can be considered negligible (not shown here).

Fractional storage in ponds drops sharply early in the melt season following initial drainage due to the melt pond–ocean connection on both MOSAiC and SHEBA. The storage continues to decrease over time on MOSAiC in contrast to SHEBA, where fractional storage somewhat rebounded following the initial drainage (Fig. 12b). The decrease on MOSAiC is in large part due to the rapidly increasing meltwater input, which outpaces the storage in ponds (which also increases; see Fig. 9). The rate of meltwater contributions were less rapid on SHEBA, and the pond storage increased somewhat more dramatically, perhaps because of the difference in ice type. The difference may be accounted for by the relatively high internal storage in FYI (Fig. 10), which was not present during SHEBA.

4.2 Variability in the sea ice freshwater balance

There is variability in the sources and sinks in the sea ice freshwater budget both within our observational dataset (local scale) and across years and locations (basin scale). Here we consider the possible errors in our estimates that may impact the results shown and discuss the variability in relevant terms that may result in a larger range of values on the basin scale. In general, we expect the fractional distribution of sinks to vary more than sources due to the significant role of atmospheric and ocean forcing on small-scale heterogeneity, and these sink estimates also have more uncertainty in our calculations.

Variability in estimated source terms for this case study may result from snow thickness (which largely determines the snowmelt input), sea ice bottom and surface melt, ridge fraction and thickness ratio, lateral melt rate, sea ice salinity, and liquid precipitation rate. Transect observations gave pre-melt (May) snow thickness of 31 ± 17 cm (Itkin et al., 2023), which suggests up to almost 50 % variability in the local snowmelt contribution. Similarly, sea ice bottom and surface melt rates vary significantly by thickness and ice type across the floe (Raphael et al., 2024), but the relative agreement across methods suggests the average contributions have errors less than 10 % (Fig. 3). Sea ice core salinity values ranged from 1–5 g kg^{-1} (Angelopoulos et al., 2022; Salganik et al., 2023a). Sea ice and density used in the volume conversions may present another possible source of error (Salganik et al., 2024) but are estimated to be small compared to other listed terms. Error and variability in lateral melt rate cannot be estimated from the observations available, but the relative magnitude is likely to be most sensitive to the size of the floe considered in budget calculations. Precipitation esti-

mates may have substantial uncertainty, as described (Fig. 5), but should not vary spatially across the floe considered.

While the comparison with SHEBA suggests that there may be reasonable consistency in source terms across years and locations (Fig. 12), we would expect that there is significant basin-scale variability in the magnitude and fraction of sea-ice-derived freshwater. As snow on sea ice mostly melts by the end of Arctic summer, the snowmelt term is mostly bounded by the seasonal maximum snow thickness, which has been estimated pan-Arctic as 20 ± 6 cm from ICESat-2 and CryoSat-2 altimeters (Kacimi and Kwok, 2022). Variability in bottom and surface melt is at least in part determined by the ice age, which ranges from pure FYI to pure MYI across the Arctic. Coupled sea ice models may be used to explore the relative contributions from mass budget terms in the context of the freshwater budget (e.g., Keen et al., 2021), where the changes in proportions of ice types likely lead to changes in dominant melt terms. One contribution to this is the range in ridge fraction, which can be estimated as varying from 12 %–20 %, as discussed in Methods. Finally, pre-melt sea ice bulk salinity similarly varies from 1–2 g kg^{-1} for pure SYI to 4–5 g kg^{-1} for pure FYI (Vancoppenolle et al., 2009b), which may impact the conversion from sea ice meltwater to freshwater by up to 10 %.

Variability in sink terms may be a result of uncertainty in melt pond depth and fraction; melt pond salinity; depth and salinity of under-ice meltwater layers; depth of lead meltwater layers; lead or open-water fraction; and variability in terms used in internal storage estimates, including meltwater salinity, ocean reference salinity, ocean heat flux, and initial snow thickness. In general, the uncertainty in each of these terms can be expected to be large. Melt pond volumes calculated using aerial and satellite photogrammetry suggest that the transect data used here may underestimate the equivalent freshwater thickness by up to 50 % early in the time series (30 June) due to location bias, but estimates converge by mid-July because of pond drainage (Fuchs et al., 2024). Comparison of different methods for estimating under-ice and lead-layer freshwater equivalent gives estimates that vary by as much as 100 % and 50 % on a given date, respectively. Direct estimates of the uncertainty in internal storage using ranges of observed input terms (Fig. 10) give an error around 10 % for the FYI core data, but estimates vary largely by ice type and model. Thus, the ratio of sink terms is likely to have significant error and variability spatially.

As a comprehensive budget of sea ice freshwater sinks has not previously been completed, we cannot evaluate how this might vary. Melt ponds can vary widely in depth and coverage based on ice type, morphology, and forcing conditions (e.g., Buckley et al., 2020; Fetterer and Untersteiner, 1998; Webster et al., 2015, 2022). Freshwater layers under ice and in leads have been observed previously but are also commonly not present in observations made across the Arctic during the melt season (Smith et al., 2023). We suggest that future work addressing this gap is needed. Modeling studies using coupled global climate models may be well suited to address some of these questions regarding variability in meltwater storage in ponds and in the ice.

4.3 Comparison with a model: CESM2

Model representation of freshwater budget source terms from snow and sea ice meltwater and the storage in ponds is evaluated using one CMIP6-class coupled sea ice model, the Community Earth System Model 2 (CESM2; Danabasoglu et al., 2020). Model outputs are evaluated using a sea ice grid cell near the MOSAiC location, where averages over 10 years from 2015–2025 are computed (Fig. 13). The modeled total freshwater input from sea ice melt and snowmelt (Fig. 13) is moderately low compared to that observed (Fig. 7), with about 0.35 m (40 %) less total freshwater input from sea ice and snow terms. There are more significant differences when comparing individual source terms. The model predicts more bottom melt but less surface melt compared to observations. Specifically, by 25 July, there is approximately 0.1 m (50 %) more freshwater contributed from bottom melt in the model compared to the observations, while the contribution from surface melt is about 0.35 m more (around 3×) in observations compared to the model. The snowmelt and lateral ice melt are both lower in the observations than in the model. We note that MOSAiC provides only one realization of the range of possible conditions represented by the model, so future investigations with a forced 1D model will be necessary to understand the role of atmospheric or oceanic drivers versus processes in contributing to these differences.

Properly representing the storage of melt ponds in coupled climate models is critical to the representation of a number of other processes. We evaluate the representation of melt pond fractional storage in the model by calculating the fractional storage in the same manner as for observations (Fig. 13b). The model dramatically underestimates the fractional storage of surface meltwater in melt ponds, despite the underrepresentation of surface meltwater budget terms (Fig. 13a). The modeled storage never exceeds 4 %, and it peaks much later than in the observations. Additionally, the greater estimates of melt pond volume over the entire CO2 floe from orthomosaics early in the observational period (see Sect. 3.2; Fuchs et al., 2024) suggest that the observational estimates of pond storage (Figs. 9b, 13b) may be biased low, which would push the observations and model estimates even further apart. Our working hypothesis is that this is a result of vertical meltwater drainage parameterizations which result in ponds that are too thin (e.g., Webster et al., 2022). Separate ongoing work is seeking to better understand the contribution of melt pond drainage processes to pond volume and improve the representation of the meltwater budget informed by MOSAiC observations.

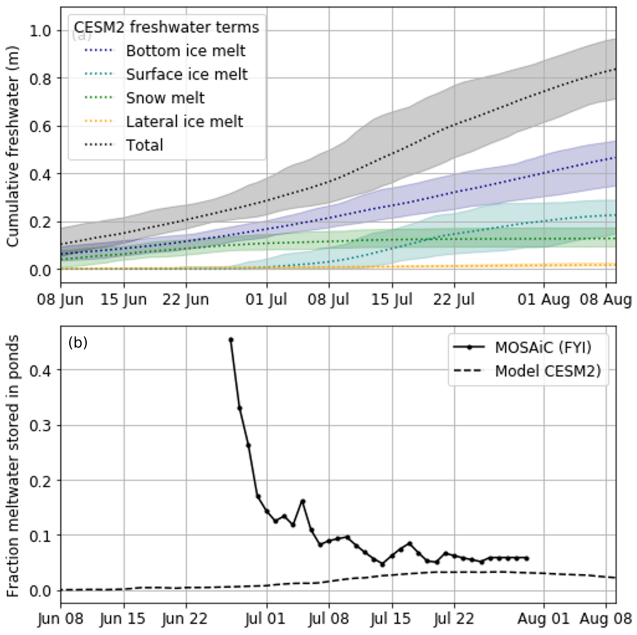

Figure 13. Sea ice freshwater budget terms from CESM2 near the MOSAiC expedition. **(a)** Freshwater source terms from sea ice melt and snowmelt, with the range over 2015–2025 in CESM2 indicated by shading. **(b)** Fractional surface freshwater stored in ponds on MOSAiC (solid) compared to model results from CESM2 over the period from 2015–2025 (dashed).

4.4 Impact on ocean heat budget

The presence of the observed thin, relatively fresh layers can have contrasting impacts on the upper-ocean heat budget driven by local solar input. On the one hand, these surface layers may accumulate solar heat which can contribute directly to enhanced lateral and basal melting (Richter-Menge et al., 2001; Smith et al., 2023). On the other hand, solar flux can also be transmitted through such thin layers, and the strongly stratified surface layer can allow solar heat to temporarily be stored deeper in the water column, inaccessible for immediate ice melt (Hudson et al., 2013; Granskog et al., 2015). Taken together, these opposing impacts suggest that the sea ice freshwater (salt) budget is closely intertwined with the upper-ocean heat budget. Small-scale processes within the mixed layer are not typically observed by oceanographic observations or represented in ocean circulation models (e.g., Steiner et al., 2004).

While we do not attempt a heat budget here, observations of upper-ocean temperature combined with rates of melting suggest some feedbacks between the two. In the ice-covered portion of the study area, transmitted energy is likely directly available for sea ice bottom melt on the order of centimeters (Tao et al., 2024). In the open-water portion (leads), the solar heating can be directly available for lateral melt. The heat available for melting is determined as a function of the temperature difference of the water from freezing, following Richter-Menge et al. (2001):

$$Q = \rho_{\mathrm{fw}} c_{\mathrm{fw}} (T - T_{\mathrm{f}}) \Delta z, \tag{7}$$

where ρ_{fw} is the freshwater density; c_{fw} is the specific heat capacity of freshwater, $4185\,\mathrm{J\,kg^{-1}\,K^{-1}}$; Δz is the depth range of the layer; and $T - T_{\mathrm{f}}$ is the difference between the water temperature and the salinity-determined freezing point. This is calculated here over the upper 2 m ($\Delta z = 2$) of leads using near-surface ocean profiles made on six dates in July (Smith et al., 2021a), shown in Fig. 14. The salinity-determined freezing point is calculated using the Gibbs Seawater implementation of the Thermodynamic Equation of Seawater 2010 (TEOS-10) (McDougall and Barker, 2011). The lower salinity of the layer results in higher relative heat content for the same temperature. While there are lower-salinity layers present near the surface on all dates (Fig. 14b), the temperature above freezing is highest at above 2 °C on 1 July and typically below 1 °C after that (Fig. 14a). This results in a high heat content initially, which may have contributed to the initial increase in lateral melt rates (e.g., Fig. 7), which then stays at a relatively constant level for the remainder of the observation period.

The net impact of the freshwater budget on the heat budget cannot be determined, especially as the total solar heat flux is larger than the ocean heat flux from lateral and basal melt (e.g., Hudson et al., 2013). Regardless, observations suggest that the interaction of the two can increase lead heat content and lateral melt rates, which may persist throughout the melt season once initiated.

4.5 Meltwater composition from isotopic analysis

The oxygen isotope ratio and salinity of seawater may be used to differentiate sources as meteoric water (river runoff and precipitation) from sea ice meltwater (e.g., Macdonald et al., 1995). Isotopic analysis (δ^{18}O) was undertaken as part of the MOSAiC expedition to understand freshwater sources, and results relevant to the present article can be found in Smith et al. (2022b) and Mellat et al. (2024). Smith et al. (2022b) reported that melt ponds observed on 25 July 2020 were a majority FYI melt, with a significant secondary contribution from snowmelt (Lange et al., 2022). The additional melt pond samples reported in Mellat et al. (2024) unfortunately did not have corresponding salinities recorded, so a composition analysis is not possible. Under-ice meltwater layer composition largely matched that of melt ponds (Smith et al., 2022b), consistent with the story that they are driven primarily by vertical drainage rather than bottom melt. Under-ice meltwater layers were 31 % seawater on average, suggesting some mixing between the meltwater layers and the underlying ocean by the sampling date on 25 July. Relatedly, the incorporation of snow and sea ice meltwater into the upper ocean (e.g., V_{uo}) contributes to significant changes in salinity and isotopic composition of surface seawater during the summer (Mellat et al., 2024). We also note that FYI

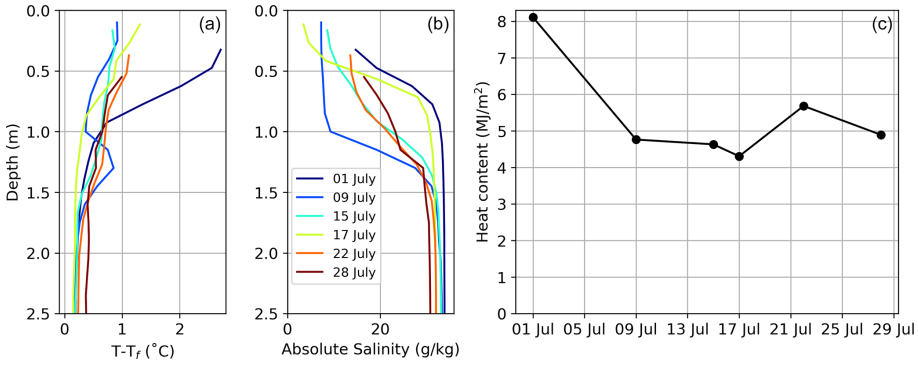

Figure 14. Upper-ocean lead profiles of **(a)** temperature above freezing and **(b)** absolute salinity on six dates in July measured using the CastAway CTD. **(b)** Lead heat content calculated by Eq. (7) on those six dates.

has a relatively high enrichment of $\delta^{18}O$ compared to SYI. This difference is likely due to modification from the longer freeze–melt history and the lower values in surface seawater (Mellat et al., 2024).

5 Conclusions

This study builds on the results of Perovich et al. (2021), who examined meltwater budgets in the Western Arctic about 20 years prior (SHEBA), to provide the first comprehensive freshwater budget of FYI and SYI from observations and quantification of the sinks. In general, there has been less deformed ice in the Arctic since 2007 (Sumata et al., 2023). As such, the substantially deformed floe measured during MOSAiC is not necessarily representative of the meltwater budget and partitioning of Arctic sea ice as a whole. However, comparison to meltwater budgets from SHEBA shows overall remarkable similarity between the source terms and melt pond storage. While these campaigns still only represent two discrete points in space and time, they can more robustly suggest some likely targets for model representation improvement, such as the storage of surface meltwater in melt ponds.

The largest source of local freshwater in the MOSAiC observations is from surface sea ice melt. Tao et al. (2024) found that a majority of solar energy input over sea ice during MOSAiC is absorbed within the ice, snow, and melt ponds rather than transmitted through to the ocean, likely contributing to accelerated surface melt rates. This suggests the potential for feedbacks between the production of freshwater (as from melt) and storage in melt ponds, which modify the solar radiative budget. In comparison, bottom melt of sea ice constituted only around one-third of cumulative freshwater in observations but was notably increased by over one-third by making adjustments for ridge fraction, which are underrepresented by typical observational methods. Precipitation sources in general are a small contribution to the freshwater budget ($< 10\,\%$ total), and the contribution from precipitation over the year stored as snow is much greater than that occurring directly during the summer as rain. As the Arctic transitions to be more rain-dominated in the future (Bintanja and Andry, 2017), the cumulative summer freshwater generation from snow will likely decrease, with a larger role for in situ precipitation. Lateral melt is a small freshwater source term on the relatively large floe observed here, as is typical within the pack ice, but is likely to be a larger contribution in marginal ice zones where typical floe sizes are smaller (e.g., Smith et al., 2022a).

The small total volume of freshwater sinks on, in, and under sea ice relative to the sources suggests that most freshwater ends up in the upper ocean. Even if we assume that errors in sink terms could be as large as $100\,\%$, the ocean would remain at least the largest freshwater sink term, if not still the majority of the volume. More direct quantification of the upper-ocean entrainment term in future studies would be useful for understanding the contribution to ocean freshening. Regardless, the storage of freshwater from sea ice melt and snowmelt has significant local impacts.

Despite their low volume, meltwater layers in ponds and in the ocean under the ice and in leads have extensive importance for the coupled Arctic system (Smith et al., 2023), acting as a barrier on the upper ocean, resulting in reduced gas and momentum exchange, separation of ecosystems, and more. Understanding the factors in formation and dissolution of these layers is key to understanding the importance across the changing Arctic. Observations from the MOSAiC expedition here show that, while a higher fraction of surface freshwater is initially retained in melt ponds on FYI, SYI stores a higher fraction of freshwater through the mid- to late summer. This is likely in part a result of the evolution of fractional coverage of melt ponds. Recent research has similarly suggested that melt pond fraction is initially higher on less deformed ice but remains higher later in the summer on more deformed ice (Niehaus et al., 2024), likely due to a reduction both in lateral drainage, as a result of the surface expression of deformation, and in vertical drainage, related to reduced permeability with lower salinities. However, contradictory results throughout the literature suggest that this

could be an important topic to address with future research (Polashenski et al., 2012; Webster et al., 2015; Buckley et al., 2020; Webster et al., 2022). An additional novel result of this study is that internal storage of freshwater in the sea ice through the desalinization process is larger than other quantified sinks. The associated brine drainage to the ocean results in a salinification of the upper ocean at the same time that melt is directly freshening, making observational constraint of the freshwater budget in the ocean even more challenging.

Appendix A: Open-water fraction estimates

Figure A1 summarizes the methods related to the calculation of open-water fraction. The area over which open-water fraction is calculated from orthomosaics (Neckel et al., 2023) is shown in the images in the top row, with shaded red rings. The sea-ice-covered fraction, where the open-water fraction is 1 minus the sea ice fraction, is plotted in the bottom panel in red, which is interpolated to dates between. For context, they are compared with two satellite methods for estimated sea-ice-covered fraction, which generally bracket the same range of values, giving higher confidence to the estimates.

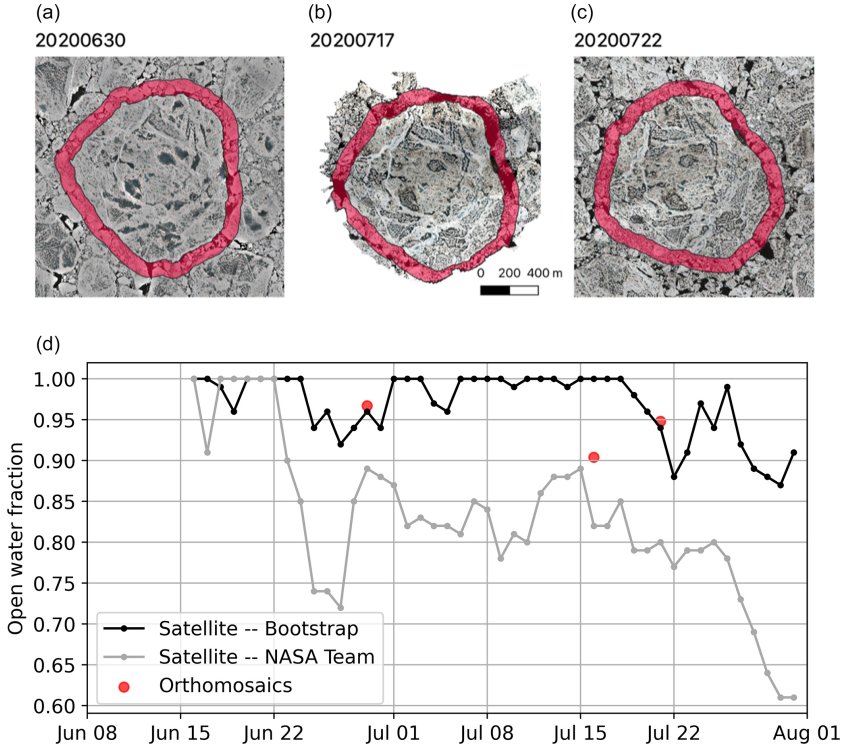

Figure A1. Methods for calculation of the open-water fraction. Panels **(a)–(c)** show aerial orthomosaic maps (from Neckel et al., 2023) of the floe area and the 100 m ring around the floe used to determine the open-water fraction on three dates. Panel **(d)** shows a comparison of the open-water fraction (derived from the top images; red circles) with satellite sea ice products (which have a spatial resolution of 25 km × 25 km).

Appendix B: Upper ocean (V_{uo})

The freshwater content of the upper ocean h_{FW} can be calculated from profiles of vertical absolute salinity S_A by integrating the deviation in salinity from a chosen reference salinity S_{ref} over some vertical range z_t to z_b,

$$h_{FW} = \int_{z_t}^{z_b} \frac{S_{ref} - S}{S_{ref}} dz, \tag{B1}$$

following, e.g., Rabe et al. (2011). Here, we calculated h_{FW} from daily averaged salinity profiles obtained with a microstructure profiler at a central position of the MOSAiC floe (Ocean City; Schulz et al., 2022). Several profiles were measured on a near-daily basis through a hole in the sea ice between 27 June and 29 July 2020, with no data available on 12, 23, and 24 July 2020. In contrast to hydrographic measurements performed from the ship, which are affected by mixing created at the ship's keel and by its positioning system, the microstructure measurements represent a more undisturbed upper-ocean stratification. Vertical integration was chosen to start at $z_t = 4$ m to avoid including salinity measurements in a freshwater lens that was present at the sampling site until mid-June 2020. The lower limit was either chosen as a fixed depth level (50 m) or a fixed isohaline (32.4 g kg^{-1}), and the reference salinity was chosen to be 34.2 g kg^{-1}. Results are insensitive to the choice of the lower integration threshold criterion and variations of the exact depth level or isohaline, except towards the end of July (see Fig. B1b), when the 34.2 g kg^{-1} isohaline had deepened from initially between 4–60 m to over 100 m. Results are quantitatively more sensitive to the choice of reference salinity; however, the qualitative behavior of h_{FW} holds for a broader variation in S_{ref}.

Ignoring the presence of lateral gradients or advective effects, the evolution of h_{FW} would reflect the input of freshwater into the upper ocean. However, the drift traversed substantial lateral salinity gradients associated with entering the edge of the transpolar drift of river-rich water on 16 July 2020 when leaving the Yermak Plateau and with the subsequent progression further into the low-salinity core (vertical dashed line, Fig. B1a). This transition into a different surface water regime is also visible in other parameters than salinity, i.e., an increase in the river water fraction (based on oxygen isotope measurements) and a higher concentration of colored dissolved organic matter characteristic of river water (see Schulz et al., 2024). The evolution of h_{FW} after 16 July 2020 is therefore dominated by regional gradients in surface salinity and does not provide means to discern local meltwater input into the upper ocean.

Between 27 June and 16 July 2020, we did not observe any changes in upper-ocean properties that point to pronounced lateral gradients. For this period of time, we can assume the variability in h_{FW} reflects meltwater input, acknowledging that this involves the assumption of no lateral effects, which cannot be proven. Ocean freshwater content exhibited little variability until 11 July, with values ranging between 0.1–0.2 m before 6 July 2020 and 0.2–0.3 m after. Sometime between 11–13 July, freshwater content increased by around 0.35 to 0.6 m, likely associated with the substantial melt pond drainage event (Webster et al., 2022) and vertical mixing events which redistributed meltwater from a shallow, meter-scale layer near the surface through the upper tens of meters in the ocean. A subsequent slight decrease in h_{FW} of 0.1 m over 3 d could be attributed to a lateral spreading of the localized meltwater input driven by baroclinic instabilities.

Overall, we conclude that, in our case, the upper-ocean freshwater content by itself is not suited to quantify meltwater input into the ocean. The contribution of spatial gradients or lateral advection cannot be isolated from the meltwater input and might dominate the signal, especially near hydrographic fronts.

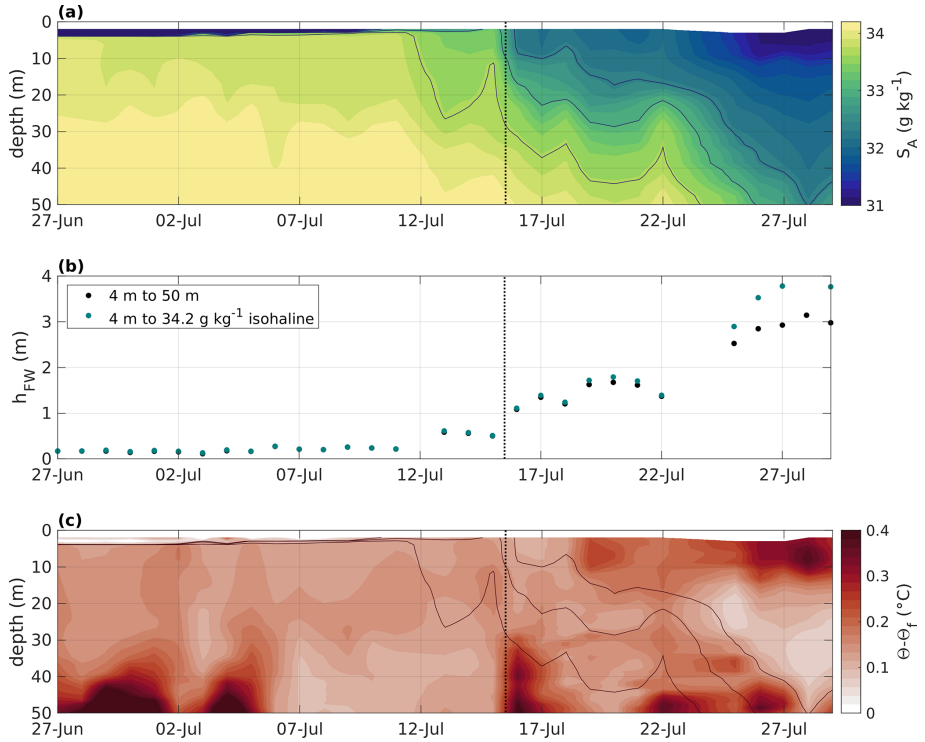

Figure B1. Time series of **(a)** upper-ocean absolute salinity (g kg^{-1}), **(b)** freshwater content (meters), and **(c)** conservative temperature Θ deviation from freezing temperature Θ_f (°C). Dashed vertical lines indicate the timing of the front between surface regimes that are rich and poor in river water.

Appendix C: Internal storage

Figure C1 compares vertical profiles of salinity estimates from IMB buoys in FYI and SYI (left and middle panels) and the resulting change in salt mass over time (right panel). The salt mass, $m_S = S_{si} \cdot h_{si}\mathrm{rho}_{si}$, decreases from the start of the melt season onwards. Figure C2 then compares bulk brine volume estimates from coring measurements (circles) and from IMB buoys near coring sites (dashed lines). The relative volume of brine was estimated using ice salinity and temperature measurements (Fig. C3) from ice coring using Cox and Weeks (1983) for cold ice and Leppäranta and Manninen (1988) for ice warmer than -2 °C. We note that the bulk ice temperature is notably warmer for FYI in much of July (Fig. C3) due to the presence of thin meltwater layers, which also impacts the simulated brine volume. To fill the observational gap between 4 May and 22 June, brine volume was also estimated using temperature measurements from two IMB buoys located near coring FYI and SYI sites, with linearly interpolated salinity from ice coring. The close agreement in magnitude and approximate timing suggests that coring observations provide a reasonable estimate of salt mass flux from the ice on both FYI and SYI.

Bulk ridge salinities (Fig. C4) show general freshening trends of ridges over time. These generally follow the freshening trends of level FYI and SYI (e.g., Fig. C1) and support the approach of estimating combined internal meltwater storage.

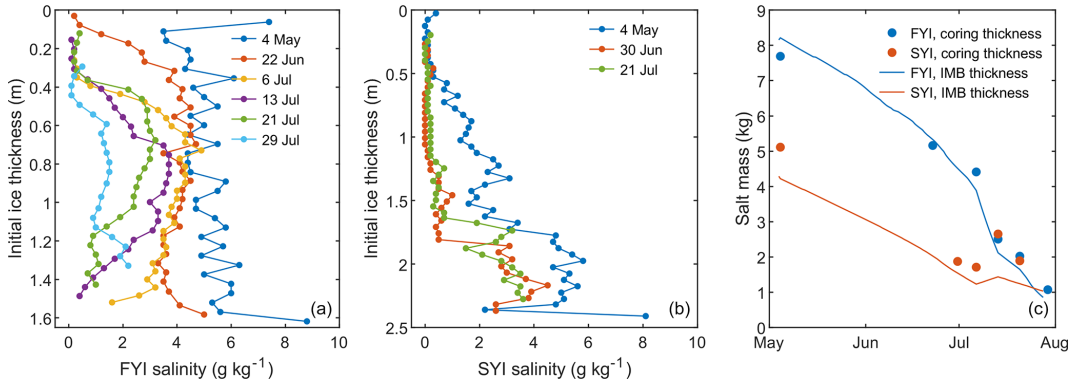

Figure C1. Vertical profiles of first- **(a)** and second-year ice salinity **(b)** and the temporal evolution of salt mass of first- and second-year ice.

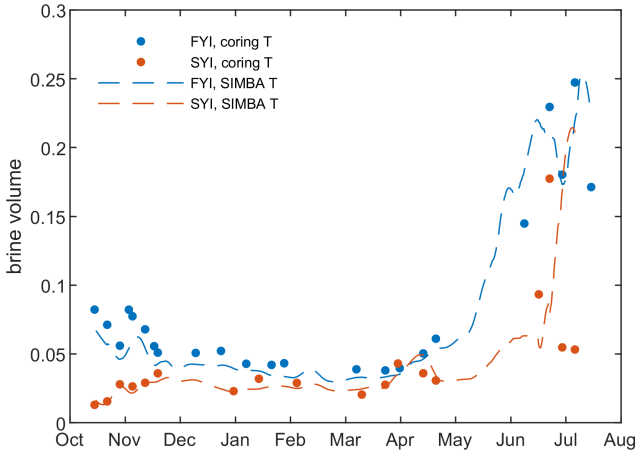

Figure C2. Bulk brine volume for level FYI (blue) and SYI (red) from cores (circles) and IMB buoys (dashed lines).

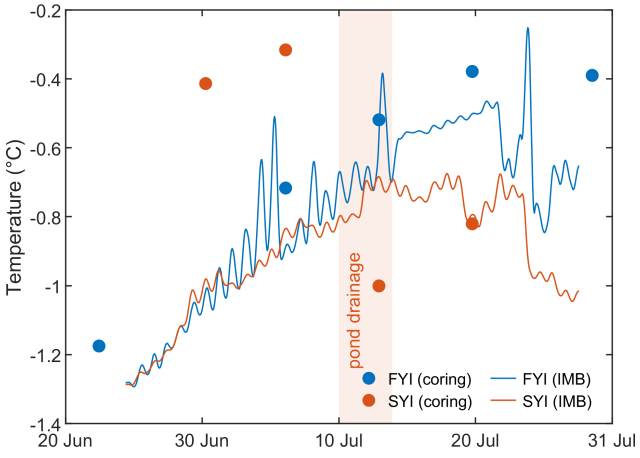

Figure C3. Bulk ice temperature for level FYI (blue) and SYI (red) from cores (circles) and IMBs (lines).

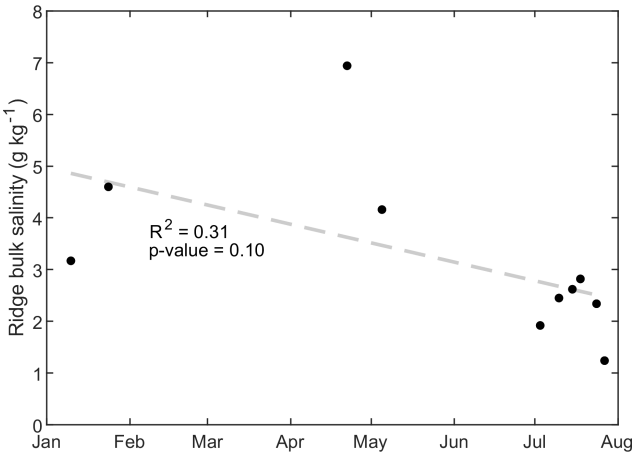

Figure C4. Bulk salinity of various ridges sampled within CO1.

Data availability. All MOSAiC datasets used have been archived and are available as follows:

- Stakes data: Raphael et al. (2022);
- IMB datasets: several datasets were used in this analysis, including SIMB archived at https://doi.org/10.18739/A20Z70Z01 (Perovich et al., 2022); DTCs archived at https://doi.org/10.1594/PANGAEA.964023 (Salganik et al., 2023d); and SIMBAs, which are individually archived with the following DOIs: https://doi.org/10.1594/PANGAEA.940393 (T58) (Lei et al., 2022a), https://doi.org/10.1594/PANGAEA.940231 (T62) (Lei et al., 2022b), https://doi.org/10.1594/PANGAEA.940593 (T63) (Lei et al., 2022c), https://doi.org/10.1594/PANGAEA.940617 (T64) (Lei et al., 2022d), https://doi.org/10.1594/PANGAEA.938134 (T66) (Lei et al., 2021a), https://doi.org/10.1594/PANGAEA.938128 (T67) (Lei et al., 2021b), https://doi.org/10.1594/PANGAEA.940659 (T70) (Lei et al., 2022e), https://doi.org/10.1594/PANGAEA.940692 (T74) (Lei et al., 2022f), https://doi.org/10.1594/PANGAEA.940740 (T75) (Lei et al., 2022g), https://doi.org/10.1594/PANGAEA.940702 (T76) (Lei et al., 2022h), and https://doi.org/10.1594/PANGAEA.940712 (T79) (Lei et al., 2022i);
- Floe orthomosaics: Neckel et al. (2023);
- Snow freeboard from airborne laser scanner: https://doi.org/10.1594/PANGAEA.950896 (Hutter et al., 2023);
- Precipitation datasets: Kyrouac and Holdridge (2019);
- Melt ponds: https://doi.org/10.1594/PANGAEA.937781 (Itkin et al., 2021);
- Melt pond salinities: Lange et al. (2022);
- YSI lead and under-ice: Smith et al. (2021a);
- Fishing rod CTD: https://doi.org/10.1594/PANGAEA.956142 (Karam et al., 2023);
- Coring: https://doi.org/10.1594/PANGAEA.956732 (Oggier et al., 2023a), https://doi.org/10.1594/PANGAEA.959830 (Oggier et al., 2023b);
- Upper ocean: https://doi.org/10.18739/A2TT4FV1G (Smith et al., 2021a);
- SHEBA mass balance data: Perovich et al. (2007).

Author contributions. MMS conceptualized the study. MMS, NF, DKP, IR, ES, MAG, KS, MDS, and MW curated data for analysis, and MMS, ES, NF, and KS contributed to formal analysis. MMS, NF, and KS contributed to visualization. MMS led writing of the draft, with all authors contributing and approving the final draft. Funding acquisition: MMS, MAG, and KS.

Competing interests. The contact author has declared that none of the authors has any competing interests.

Disclaimer. Publisher's note: Copernicus Publications remains neutral with regard to jurisdictional claims made in the text, published maps, institutional affiliations, or any other geographical representation in this paper. While Copernicus Publications makes every effort to include appropriate place names, the final responsibility lies with the authors.

Acknowledgements. Madison M. Smith was supported by NSF OPP 2138787. Evgenii Salganik and Mats A. Granskog were supported by the Research Council of Norway project HAVOC (grant no 280292), and Evgenii Salganik was supported by project INTERAAC (grant no. 328957). Mats A. Granskog acknowledges support from the Hanse-Wissenschaftskolleg Institute of Advanced Study (Delmenhorst, Germany) and funding from the European Union's Horizon 2020 research and innovation program under grant no. 101003826 via project CRiceS (Climate-relevant interactions and feedbacks: the key role of sea ice and snow in the polar and global climate system). Kirstin Schulz received support from the National Science Foundation, grant no. NSF-OCE-2401413. Niels Fuchs acknowledges funding from the BMBF project NiceLABpro (03F0867A) and from the Deutsche Forschungsgemeinschaft under Germany's Excellence Strategy (EXC 2037; Climate, Climatic Change, and Society (CLICCS); project no. 390683824). Melinda Webster conducted this work under the NSF project 2325430 and NASA's Interdisciplinary Research in Earth Science project 80NSSC21K0264. Matthew D. Shupe was supported by the U.S. Department of Energy (DOE; DE-SC0021341), the NOAA Physical Sciences Laboratory (NA22OAR4320151), and the Global Ocean Monitoring and Observing Program (FundRef https://doi.org/10.13039/100018302). Ian A. Raphael was supported by NSF OPP-1724540 and NSF OPP-1724424.

Data used in this article were produced as part of the international Multidisciplinary drifting Observatory for the Study of the Arctic Climate (MOSAiC) with the tag MOSAiC20192020 and the Project_ID AWI_PS122_00. We thank all people involved in the expedition of R/V *Polarstern* Knust (2017) during MOSAiC in 2019–2020 as listed in Nixdorf et al. (2021). Precipitation data were obtained from the Atmospheric Radiation Measurement (ARM) User Facility, a DOE Office of Science user facility managed by the Biological and Environmental Research program. We acknowledge Dave Bailey and Marika Holland for assistance with CESM2 out-

puts. The CESM project is supported primarily by the National Science Foundation. Computing and data storage resources, including the Cheyenne supercomputer (https://doi.org/10.5065/D6RX99HX, Computational and Information Systems Laboratory, 2019), were provided by the Computational and Information Systems Laboratory (CISL) at NCAR.

Financial support. This research has been supported by the Directorate for Geosciences (grant nos. 2138787, 2401413, 2325430, 1724540, and 1724424), the Norges Forskningsråd (grant no. 280292 and 328957), the Bundesministerium für Bildung und Forschung (grant no. 03F0867A), the Deutsche Forschungsgemeinschaft (grant no. 390683824), the National Aeronautics and Space Administration (grant no. 80NSSC21K0264), the U.S. Department of Energy (grant no. DE-SC0021341), the National Oceanic and Atmospheric Administration (grant no. NA22OAR4320151), and European Union's Horizon 2020 (grant no. 101003826).

Review statement. This paper was edited by Stephen Howell and reviewed by Cathleen Geiger and Peng Lu.

References

Aagaard, K. and Carmack, E. C.: The role of sea ice and other fresh water in the Arctic circulation, J. Geophys. Res.-Oceans, 94, 14485–14498, 1989.

Alexandrov, V., Sandven, S., Wahlin, J., and Johannessen, O. M.: The relation between sea ice thickness and freeboard in the Arctic, The Cryosphere, 4, 373–380, https://doi.org/10.5194/tc-4-373-2010, 2010.

Angelopoulos, M., Damm, E., Simões Pereira, P., Abrahamsson, K., Bauch, D., Bowman, J., Castellani, G., Creamean, J., Divine, D. V., Dumitrascu, A., Fons, S. W., Granskog, M. A., Kolabutin, N., Krumpen, T., Marsay, C., Nicolaus, M., Oggier, M., Rinke, A., Sachs, T., Shimanchuk, E., Stefels, J., Stephens, M., Ulfsbo, A., Verdugo, J., Wang, L., Zhan, L., and Haas, C.: Deciphering the Properties of Different Arctic Ice Types During the Growth Phase of MOSAiC: Implications for Future Studies on Gas Pathways, Front. Earth Sci., 10, 864523, https://doi.org/10.3389/feart.2022.864523, 2022.

Ardyna, M. and Arrigo, K. R.: Phytoplankton dynamics in a changing Arctic Ocean, Nat. Clim. Change, 10, 892–903, 2020.

Bintanja, R. and Andry, O.: Towards a rain-dominated Arctic, Nat. Clim. Change, 7, 263–267, 2017.

Buckley, E. M., Farrell, S. L., Duncan, K., Connor, L. N., Kuhn, J. M., and Dominguez, R. T.: Classification of sea ice summer melt features in high-resolution IceBridge imagery, J. Geophys. Res.-Oceans, 125, e2019JC015738, https://doi.org/10.1029/2019JC015738, 2020.

Chamberlain, E. J.: Microbial contributions to metabolic oxygen turnover in the central Arctic Ocean, University of California San Diego, https://escholarship.org/uc/item/0k0439q9 (last access: 31 January 2025), 2023.

Chandra, A., Zhang, C., Kollias, P., Matrosov, S., and Szyrmer, W.: Automated rain rate estimates using the Ka-band ARM zenith radar (KAZR), Atmos. Meas. Tech., 8, 3685–3699, https://doi.org/10.5194/amt-8-3685-2015, 2015.

Comiso, J. C.: Bootstrap Sea Ice Concentrations from Nimbus-7 SMMR and DMSP SSM/I-SSMIS, Version 2 [data set], https://doi.org/10.5067/X5LG68MH013O, 2000.

Computational and Information Systems Laboratory: Cheyenne: HPE/SGI ICE XA System (NCAR Community Computing), Boulder, CO, National Center for Atmospheric Research, https://doi.org/10.5065/D6RX99HX, 2019.

Cox, C., Gallagher, M., Shupe, M., Persson, O., B. Blomquist and, A. G., Riihimaki, L., Kutchenreiter, M., Morris, V., Solomon, A., Brooks, I., Costa, D., Gottas, D., Hutchings, J., Osborn, J., Morris, S., Preusser, A., and Uttal, T.: Met City meteorological and surface flux measurements (Level 3 Final), Multidisciplinary Drifting Observatory for the Study of Arctic Climate (MOSAiC), central Arctic, October 2019–September 2020, Arctic Data Center [data set], https://doi.org/10.18739/A2PV6B83F, 2023.

Cox, G. F. N. and Weeks, W. F.: Equations for Determining the Gas and Brine Volumes in Sea-Ice Samples, J. Glaciol., 29, 306–316, https://doi.org/10.3189/S0022143000008364, 1983.

Danabasoglu, G., Lamarque, J.-F., Bacmeister, J., et al.: The Community Earth System Model version 2 (CESM2), J. Adv. Model. Earth Sy., 12, e2019MS001916, https://doi.org/10.1029/2019MS001916, 2020.

DiGirolamo, N. E., Parkinson, C. L., Cavalieri, D. J., Gloersen, P., and Zwally, H. J.: Sea Ice Concentrations from Nimbus-7 SMMR and DMSP SSM/I-SSMIS Passive Microwave Data, Version 2 [data set], https://doi.org/10.5067/MPYG15WAA4WX, 2022.

Ehn, J. K., Mundy, C., Barber, D. G., Hop, H., Rossnagel, A., and Stewart, J.: Impact of horizontal spreading on light propagation in melt pond covered seasonal sea ice in the Canadian Arctic, J. Geophys. Res.-Oceans, 116, C00G02, https://doi.org/10.1029/2010JC006908, 2011.

Eicken, H.: Structure of under-ice melt ponds in the central Arctic and their effect on, the sea-ice cover, Limnol. Oceanogr., 39, 682–693, 1994.

Fetterer, F. and Untersteiner, N.: Observations of melt ponds on Arctic sea ice, J. Geophys. Res.-Oceans, 103, 24821–24835, 1998.

Fuchs, N.: A multidimensional analysis of sea ice melt pond properties from aerial images, Universität Bremen, PhD dissertation, https://doi.org/10.26092/elib/2249, 2023.

Fuchs, N., von Albedyll, L., Birnbaum, G., Linhardt, F., Oppelt, N., and Haas, C.: Sea ice melt pond bathymetry reconstructed from aerial photographs using photogrammetry: a new method applied to MOSAiC data, The Cryosphere, 18, 2991–3015, https://doi.org/10.5194/tc-18-2991-2024, 2024.

Gradinger, R., Bluhm, B., and Iken, K.: Arctic sea-ice ridges – Safe heavens for sea-ice fauna during periods of extreme ice melt?, Deep-Sea Res. Pt. II, 57, 86–95, 2010.

Granskog, M. A., Pavlov, A. K., Sagan, S., Kowalczuk, P., Raczkowska, A., and Stedmon, C. A.: Effect of sea–ice melt on inherent optical properties and vertical distribution of solar radiant heating in Arctic surface waters, J. Geophys. Res.-Oceans, 120, 7028–7039, https://doi.org/10.1002/2015JC011087, 2015.

Griewank, P. J. and Notz, D.: Insights into brine dynamics and sea ice desalination from a 1-D model study of gravity drainage, J. Geophys. Res.-Oceans, 118, 3370–3386, 2013.

Guo, W., Itkin, P., Singha, S., Doulgeris, A. P., Johansson, M., and Spreen, G.: Sea ice classification of TerraSAR-X ScanSAR images for the MOSAiC expedition incorporating per-class incidence angle dependency of image texture, The Cryosphere, 17, 1279–1297, https://doi.org/10.5194/tc-17-1279-2023, 2023.

Guzenko, R. B., Mironov, Y. U., May, R. I., Porubaev, V. S., Kovalev, S. M., Khotchenkov, S. V., Kornishin, K. A., and Efimov, Y.: Morphometry and Internal Structure of Ice Ridges and Stamukhas in the Kara, Laptev and East Siberian Seas. Results of 2013–2017 Field Studies, SSRN, https://doi.org/10.2139/ssrn.4359510, 2023.

Haine, T. W., Curry, B., Gerdes, R., Hansen, E., Karcher, M., Lee, C., Rudels, B., Spreen, G., de Steur, L., Stewart, K. D., and Woodgate, R.: Arctic freshwater export: Status, mechanisms, and prospects, Global Planet. Change, 125, 13–35, 2015.

Hersbach, H., Bell, B., Berrisford, P., Hirahara, S., Horányi, A., Muñoz-Sabater, J., Nicolas, J., Peubey, C., Radu, R., Schepers, D., Simmons, A., Soci, C., Abdalla, S., Abellan, X., Balsamo, G., Bechtold, P., Biavati, G., Bidlot, J., Bonavita, M., Chiara, G. D., Dahlgren, P., Dee, D., Diamantakis, M., Dragani, R., Flemming, J., Forbes, R., Fuentes, M., Geer, A., Haimberger, L., Healy, S., Hogan, R., Hólm, E., Janisková, M., Keeley, S., Laloyaux, P., Lopez, P., Lupu, C., Radnoti, G., de Rosnay, P., Rozum, I., Vamborg, F., Villaume, S., and Thépaut, J.-N.: Complete ERA5 from 1940: Fifth generation of ECMWF atmospheric reanalyses of the global climate, Copernicus Climate Change Service (C3S) Data Store (CDS) [data set], https://doi.org/10.24381/cds.143582cf, 2017.

Hudson, S. R., Granskog, M. A., Sundfjord, A., Randelhoff, A., Renner, A. H. H., and Divine, D. V.: Energy budget of first-year Arctic sea ice in advanced stages of melt, Geophys. Res. Lett., 40, 2679–2683, https://doi.org/10.1002/grl.50517, 2013.

Hutter, N., Hendricks, S., Jutila, A., Ricker, R., von Albedyll, L., Birnbaum, G., and Haas, C.: Gridded airborne laserscanner (ALS) elevation data (L4) for three flights during MOSAiC (prerelease), Zenodo [data set], https://doi.org/10.5281/zenodo.5121824, 2021.

Hutter, N., Hendricks, S., Jutila, A., Birnbaum, G., von Albedyll, L., Ricker, R., and Haas, C.: Merged grids of sea-ice or snow freeboard from helicopter-borne laser scanner during the MOSAiC expedition, version 1, PANGAEA [data set], https://doi.org/10.1594/PANGAEA.950896, 2023.

Itkin, P., Webster, M., Hendricks, S., Oggier, M., Jaggi, M., Ricker, R., Arndt, S., Divine, D., von Albedyll, L., Raphael, I., Rohde, J., and Liston, G. E.: Magnaprobe snow and melt pond depth measurements from the 2019–2020 MOSAiC expedition, PANGAEA [data set], https://doi.org/10.1594/PANGAEA.937781, 2021.

Itkin, P., Hendricks, S., Webster, M., von Albedyll, L., Arndt, S., Divine, D., Jaggi, M., Oggier, M., Raphael, I., Ricker, R., Rohde, J., Schneebeli, M., and Liston, G. E.: Sea ice and snow characteristics from year-long transects at the MOSAiC Central Observatory, Elem. Sci. Anth., 11, 00048, https://doi.org/10.1525/elementa.2022.00048, 2023.

Jackson, K., Wilkinson, J., Maksym, T., Meldrum, D., Beckers, J., Haas, C., and Mackenzie, D.: A novel and low-cost sea ice mass balance buoy, J. Atmos. Ocean. Tech., 30, 2676–2688, 2013.

Kacimi, S. and Kwok, R.: Arctic snow depth, ice thickness, and volume from ICESat-2 and CryoSat-2: 2018–2021, Geophys. Res. Lett., 49, e2021GL097448, https://doi.org/10.1029/2021GL097448, 2022.

Karam, S., Tippenhauer, S., Allerholt, J., Hoppmann, M., Koenig, Z., Muilwijk, M., Schuffenhauer, I., and Schulz, K.: Physical oceanography measurements from a hand-held CTD during Leg 4 and 5 of POLARSTERN cruise PS122 – MOSAiC, PANGAEA [data set], https://doi.org/10.1594/PANGAEA.956142, 2023.

Keen, A., Blockley, E., Bailey, D. A., Boldingh Debernard, J., Bushuk, M., Delhaye, S., Docquier, D., Feltham, D., Massonnet, F., O'Farrell, S., Ponsoni, L., Rodriguez, J. M., Schroeder, D., Swart, N., Toyoda, T., Tsujino, H., Vancoppenolle, M., and Wyser, K.: An inter-comparison of the mass budget of the Arctic sea ice in CMIP6 models, The Cryosphere, 15, 951–982, https://doi.org/10.5194/tc-15-951-2021, 2021.

Knust, R.: Polar Research and Supply Vessel POLARSTERN operated by the Alfred-Wegener-Institute, Journal of Large-Scale Research Facilities, 3, A119, https://doi.org/10.17815/jlsrf-3-163, 2017.

Kortum, K., Singha, S., Spreen, G., Hutter, N., Jutila, A., and Haas, C.: SAR deep learning sea ice retrieval trained with airborne laser scanner measurements from the MOSAiC expedition, The Cryosphere, 18, 2207–2222, https://doi.org/10.5194/tc-18-2207-2024, 2024.

Kyrouac, J. and Holdridge, D.: Surface Meteorological Instrumentation (PWD), atmospheric Radiation Measurement (ARM) user facility [data set], https://adc.arm.gov/discovery/#/results/instrument_code::pwd (last access: 28 August 2024), 2019.

Lange, B. A., Granskog, M. A., Meyer, H., Bauch, D., Smith, M. M., von Albedyll, L., Raphael, I., Matero, I., and Salganik, E.: Oxygen and hydrogen isotopic ratios from sea ice bottom, false bottom ice, under-ice meltwater layer and surface melt pond samples collected during MOSAiC leg 4 (PS122.4), http://dx.doi.org/pangaea.de/10.1594/PANGAEA (last access: 10 July 2024), 2022.

Langleben, M.: On the factors affecting the rate of ablation of sea ice, Can. J. Earth Sci., 3, 431–439, 1966.

Lei, R., Cheng, B., Hoppmann, M., and Zuo, G.: Temperature and heating induced temperature difference measurements from SIMBA-type sea ice mass balance buoy 2019T66, deployed during MOSAiC 2019/20, PANGAEA [data set], https://doi.org/10.1594/PANGAEA.938134, 2021a.

Lei, R., Cheng, B., Hoppmann, M., and Zuo, G.: Temperature and heating induced temperature difference measurements from SIMBA-type sea ice mass balance buoy 2019T67, deployed during MOSAiC 2019/20, PANGAEA, https://doi.org/10.1594/PANGAEA.938128, 2021b.

Lei, R., Cheng, B., Hoppmann, M., and Zuo, G.: Temperature and heating induced temperature difference measurements from SIMBA-type sea ice mass balance buoy 2019T58, deployed during MOSAiC 2019/20, PANGAEA [data set], https://doi.org/10.1594/PANGAEA.940393, 2022a.

Lei, R., Cheng, B., Hoppmann, M., Zuo, G., and Lan, M.: Temperature and heating induced temperature difference measurements from SIMBA-type sea ice mass balance buoy 2019T62, deployed during MOSAiC 2019/20, PANGAEA [data set], https://doi.org/10.1594/PANGAEA.940231, 2022b.

Lei, R., Cheng, B., Zuo, G., and Hoppmann, M.: Temperature and heating induced temperature difference measurements from SIMBA-type sea ice mass balance buoy 2019T63,

deployed during MOSAiC 2019/20, PANGAEA [data set], https://doi.org/10.1594/PANGAEA.940593, 2022c.

Lei, R., Cheng, B., Hoppmann, M., and Zuo, G.: Temperature and heating induced temperature difference measurements from SIMBA-type sea ice mass balance buoy 2019T64, deployed during MOSAiC 2019/20, PANGAEA [data set], https://doi.org/10.1594/PANGAEA.940617, 2022d.

Lei, R., Cheng, B., Zuo, G., Hoppmann, M., and Lan, M.: Temperature and heating induced temperature difference measurements from SIMBA-type sea ice mass balance buoy 2019T70, deployed during MOSAiC 2019/20, PANGAEA [data set], https://doi.org/10.1594/PANGAEA.940659, 2022e.

Lei, R., Hutchings, J. K., Cheng, B., and Hoppmann, M.: Temperature and heating induced temperature difference measurements from SIMBA-type sea ice mass balance buoy 2020T74, deployed during MOSAiC 2019/20, PANGAEA [data set], https://doi.org/10.1594/PANGAEA.940692, 2022f.

Lei, R., Hutchings, J. K., Cheng, B., and Hoppmann, M.: Temperature and heating induced temperature difference measurements from SIMBA-type sea ice mass balance buoy 2020T75, deployed during MOSAiC 2019/20, PANGAEA [data set], https://doi.org/10.1594/PANGAEA.940740, 2022g.

Lei, R., Hutchings, J. K., Hoppmann, M., and Yuan, Z.: Temperature and heating induced temperature difference measurements from SIMBA-type sea ice mass balance buoy 2020T76, deployed during MOSAiC 2019/20, PANGAEA [data set], https://doi.org/10.1594/PANGAEA.940702, 2022h.

Lei, R., Hutchings, J. K., Hoppmann, M., and Yuan, Z.: Temperature and heating induced temperature difference measurements from SIMBA-type sea ice mass balance buoy 2020T79, deployed during MOSAiC 2019/20, PANGAEA [data set], https://doi.org/10.1594/PANGAEA.940712, 2022i.

Leppäranta, M. and Manninen, T.: The brine and gas content of sea ice with attention to low salinities and high temperatures, http://hdl.handle.net/1834/23905 (last access: November 2024), 1988.

Light, B., Smith, M. M., Perovich, D. K., Webster, M. A., Holland, M. M., Linhardt, F., Raphael, I. A., Clemens-Sewall, D., Macfarlane, A. R., Anhaus, P., and Bailey, D.: Arctic sea ice albedo: Spectral composition, spatial heterogeneity, and temporal evolution observed during the MOSAiC drift, Elem. Sci. Anth., 10, 000103, https://doi.org/10.1525/elementa.2021.000103, 2022.

Lique, C., Holland, M. M., Dibike, Y. B., Lawrence, D. M., and Screen, J. A.: Modeling the Arctic freshwater system and its integration in the global system: Lessons learned and future challenges, J. Geophys. Res.-Biogeo., 121, 540–566, 2016.

Macdonald, R. W., Paton, D. W., Carmack, E. C., and Omstedt, A.: The freshwater budget and under-ice spreading of Mackenzie River water in the Canadian Beaufort Sea based on salinity and $^{18}O/^{16}O$ measurements in water and ice, J. Geophys. Res.-Oceans, 100, 895–919, 1995.

Macfarlane, A. R., Dadic, R., Smith, M. M., Light, B., Nicolaus, M., Henna-Reetta, H., Webster, M., Linhardt, F., Hämmerle, S., and Schneebeli, M.: Evolution of the microstructure and reflectance of the surface scattering layer on melting, level Arctic sea ice, Elem. Sci. Anth., 11, 00103, https://doi.org/10.1525/elementa.2022.00103, 2023.

Matrosov, S. Y., Shupe, M. D., and Uttal, T.: High temporal resolution estimates of Arctic snowfall rates emphasizing gauge and radar-based retrievals from the MOSAiC expedition, Elem. Sci. Anth., 10, 00101, https://doi.org/10.1525/elementa.2021.00101, 2022.

McDougall, T. J. and Barker, P. M.: Getting started with TEOS-10 and the Gibbs Seawater (GSW) oceanographic toolbox, SCOR/IAPSO WG, 127, 1–28, http://www.teos-10.org/pubs/gsw/v3_04/pdf/Getting_Started.pdf (last access: 16 November 2024), 2011.

Mchedlishvili, A., Lüpkes, C., Petty, A., Tsamados, M., and Spreen, G.: New estimates of pan-Arctic sea ice–atmosphere neutral drag coefficients from ICESat-2 elevation data, The Cryosphere, 17, 4103–4131, https://doi.org/10.5194/tc-17-4103-2023, 2023.

Mellat, M., Brunello, C. F., Werner, M., Bauch, D., Damm, E., Angelopoulos, M., Nomura, D., Welker, J. M., Schneebeli, M., Granskog, M. A., Hoerhold, M., Macfarlane, A. R., Arndt, S., and Meyer, H.: Isotopic signatures of snow, sea ice, and surface seawater in the central Arctic Ocean during the MOSAiC expedition, Elem. Sci. Anthr., 12, 00078, https://doi.org/10.1525/elementa.2023.00078, 2024.

Miller, L. A., Burgers, T. M., Burt, W. J., Granskog, M. A., and Papakyriakou, T. N.: Air–Sea CO_2 Flux Estimates in Stratified Arctic Coastal Waters: How Wrong Can We Be?, Geophys. Res. Lett., 46, 235–243, https://doi.org/10.1029/2018GL080099, 2019.

Nansen, F.: The oceanography of the North Polar Basin. The Norwegian North Polar Expedition 1893–1896, Scient. Results, 3, 1902.

Neckel, N., Fuchs, N., Birnbaum, G., Hutter, N., Jutila, A., Buth, L., von Albedyll, L., Ricker, R., and Haas, C.: Helicopter-borne RGB orthomosaics and photogrammetric digital elevation models from the MOSAiC Expedition, Scientific Data, 10, 426, https://doi.org/10.1038/s41597-023-02318-5, 2023.

Nicolaus, M., Perovich, D. K., Spreen, G., Granskog, M. A., von Albedyll, L., Angelopoulos, M., Anhaus, P., Arndt, S., Belter, H. J., Bessonov, V., Birnbaum, G., Brauchle, J., Calmer, R., Cardellach, E., Cheng, B., Clemens-Sewall, D., Dadic, R., Damm, E., de Boer, G., Demir, O., Dethloff, K., Divine, D. V., Fong, A. A., Fons, S., Frey, M. M., Fuchs, N., Gabarró, C., Gerland, S., Goessling, H. F., Gradinger, R., Haapala, J., Haas, C., Hamilton, J., Hannula, H.-R., Hendricks, S., Herber, A., Heuzé, C., Hoppmann, M., Høyland, K. V., Huntemann, M., Hutchings, J. K., Hwang, B., Itkin, P., Jacobi, H.-W., Jaggi, M., Jutila, A., Kaleschke, L., Katlein, C., Kolabutin, N., Krampe, D., Kristensen, S. S., Krumpen, T., Kurtz, N., Lampert, A., Lange, B. A., Lei, R., Light, B., Linhardt, F., Liston, G. E., Loose, B., Macfarlane, A. R., Mahmud, M., Matero, I. O., Maus, S., Morgenstern, A., Naderpour, R., Nandan, V., Niubom, A., Oggier, M., Oppelt, N., Pätzold, F., Perron, C., Petrovsky, T., Pirazzini, R., Polashenski, C., Rabe, B., Raphael, I. A., Regnery, J., Rex, M., Ricker, R., Riemann-Campe, K., Rinke, A., Rohde, J., Salganik, E., Scharien, R. K., Schiller, M., Schneebeli, M., Semmling, M., Shimanchuk, E., Shupe, M. D., Smith, M. M., Smolyanitsky, V., Sokolov, V., Stanton, T., Stroeve, J., Thielke, L., Timofeeva, A., Tonboe, R. T., Tavri, A., Tsamados, M., Wagner, D. N., Watkins, D., Webster, M., and Wendisch, M.: Overview of the MOSAiC expedition – Snow and Sea Ice, Elementa: Science of the Anthropocene, 10, 000046, https://doi.org/10.1525/elementa.2021.000046, 2022.

Niehaus, H., Spreen, G., Birnbaum, G., Istomina, L., Jäkel, E., Linhardt, F., Neckel, N., Fuchs, N., Nicolaus, M., Sperzel, T., Tao, R., Webster, M., and Wright, N. : Sea Ice Melt Pond Frac-

tion Derived From Sentinel-2 Data: Along the MOSAiC Drift and Arctic-Wide, Geophys. Res. Lett., 50, e2022GL102102, https://doi.org/10.1029/2022GL102102, 2023.

Niehaus, H., Spreen, G., Istomina, L., and Nicolaus, M.: Regional and seasonal evolution of melt ponds on Arctic sea ice, EGUsphere [preprint], https://doi.org/10.5194/egusphere-2024-3127, 2024.

Nixdorf, U., Dethloff, K., Rex, M., Shupe, M., Sommerfeld, A., Perovich, D. K., Nicolaus, M., Heuzé, C., Rabe, B., Loose, B., Damm, E., Gradinger, R., Fong, A., Maslowski, W., Rinke, A., Kwok, R., Spreen, G., Wendisch, M., Herber, A., Hirsekorn, M., Mohaupt, V., Frickenhaus, S., Immerz, A., Weiss-Tuider, K., König, B., Mengedoht, D., Regnery, J., Gerchow, P., Ransby, D., Krumpen, T., Morgenstern, A., Haas, C., Kanzow, T., Rack, F. R., Saitzev, V., Sokolov, V., Makarov, A., Schwarze, S., Wunderlich, T., Wurr, K., and Boetius, A.: MOSAiC Extended Acknowledgement, https://epic.awi.de/id/eprint/ (last access: 31 January 2025), 2021.

Norwegian Polar Institute: Freshwater flux in the Fram Strait, Environmental monitoring of Svalbard and Jan Mayen (MOSJ), https://mosj.no/en/indikator/climate/ocean/ (last access: November 2024), 2022.

Notz, D. and Worster, M. G.: Desalination processes of sea ice revisited, J. Geophys. Res.-Oceans, 114, C05006, https://doi.org/10.1029/2008JC004885, 2009.

Notz, D., McPhee, M. G., Worster, M. G., Maykut, G. A., Schlünzen, K. H., and Eicken, H.: Impact of underwater-ice evolution on Arctic summer sea ice, J. Geophys. Res.-Oceans, 108, 3223, https://doi.org/10.1029/2001JC001173, 2003.

Oggier, M., Salganik, E., Whitmore, L., Fong, A. A., Hoppe, C. J. M., Rember, R., Høyland, K. V., Divine, D. V., Gradinger, R., Fons, S. W., Abrahamsson, K., Aguilar-Islas, A. M., Angelopoulos, M., Arndt, S., Balmonte, J. P., Bozzato, D., Bowman, J. S., Castellani, G., Chamberlain, E., Creamean, J., D'Angelo, A., Damm, E., Dumitrascu, A., Eggers, S. L., Gardner, J., Grosfeld, L., Haapala, J., Immerz, A., Kolabutin, N., Lange, B. A., Lei, R., Marsay, C. M., Maus, S., Müller, O., Olsen, L. M., Nuibom, A., Ren, J., Rinke, A., Sheikin, I., Shimanchuk, E., Snoeijs-Leijonmalm, P., Spahic, S., Stefels, J., Torres-Valdés, S., Torstensson, A., Ulfsbo, A., Verdugo, J., Vortkamp, M., Wang, L., Webster, M., Wischnewski, L., and Granskog, M. A.: First-year sea-ice salinity, temperature, density, oxygen and hydrogen isotope composition from the main coring site (MCS-FYI) during MOSAiC legs 1 to 4 in 2019/2020, PANGAEA [data set], https://doi.org/10.1594/PANGAEA.956732, 2023a.

Oggier, M., Salganik, E., Whitmore, L., Fong, A. A., Hoppe, C. J. M., Rember, R., Høyland, K. V., Gradinger, R., Divine, D. V., Fons, S. W., Abrahamsson, K., Aguilar-Islas, A. M., Angelopoulos, M., Arndt, S., Balmonte, J. P., Bozzato, D., Bowman, J. S., Castellani, G., Chamberlain, E., Creamean, J., D'Angelo, A., Damm, E., Dumitrascu, A., Eggers, L., Gardner, J., Grosfeld, L., Haapala, J., Immerz, A., Kolabutin, N., Lange, B. A., Lei, R., Marsay, C. M., Maus, S., Olsen, L. M., Müller, O., Nuibom, A., Ren, J., Rinke, A., Sheikin, I., Shimanchuk, E., Snoeijs-Leijonmalm, P., Spahic, S., Stefels, J., Torres-Valdés, S., Torstensson, A., Ulfsbo, A., Verdugo, J., Vortkamp, M., Wang, L., Webster, M., Wischnewski, L., and Granskog, M. A.: Second-year sea-ice salinity, temperature, density, oxygen and hydrogen isotope composition from the main coring site (MCS-SYI) during MOSAiC legs 1 to 4 in 2019/2020, PANGAEA [data set], https://doi.org/10.1594/PANGAEA.959830, 2023b.

Oppelt, N. and Linhardt, F.: Hyperspectral raw data (cau_stickle_1) from sea ice melt ponds during legs 4 and 5 of the MOSAiC expedition with R/V POLARSTERN, PANGAEA [data set], https://doi.org/10.1594/PANGAEA.955779, 2023.

Perovich, D., Grenfell, T., Light, B., Richter-Menge, J., Tucker, W., and Eicken, H.: Ice Mass Balance, Version 1.0 [data set], https://doi.org/10.5065/D6H130DF, 2007.

Perovich, D., Smith, M., Light, B., and Webster, M.: Meltwater sources and sinks for multiyear Arctic sea ice in summer, The Cryosphere, 15, 4517–4525, https://doi.org/10.5194/tc-15-4517-2021, 2021.

Perovich, D., Raphael, I., Moore, R., Clemens-Sewall, D., Polashenski, C., and Planck, C.: Measurements of ice mass balance and temperature from autonomous Seasonal Ice Mass Balance buoys in the Arctic Ocean, Arctic Data Center [data set], https://doi.org/10.18739/A20Z70Z01, 2022.

Perovich, D., Raphael, I., Moore, R., Clemens-Sewall, D., Lei, R., Sledd, A., and Polashenski, C.: Sea ice heat and mass balance measurements from four autonomous buoys during the MOSAiC drift campaign, Elementa: Science of the Anthropocene, 11, 00017, https://doi.org/10.1525/elementa.2023.00017, 2023.

Perovich, D. K. and Richter-Menge, J. A.: Regional variability in sea ice melt in a changing Arctic, Philos. T. R. Soc. A, 373, 20140165, https://doi.org/10.1098/rsta.2014.0165, 2015.

Perovich, D. K., Grenfell, T. C., Light, B., and Hobbs, P. V.: Seasonal evolution of the albedo of multiyear Arctic sea ice, J. Geophys. Res.-Oceans, 107, 1–20, https://doi.org/10.1029/2000JC000438, 2002.

Perovich, D. K., Grenfell, T. C., Richter-Menge, J. A., Light, B., Tucker, W. B., and Eicken, H.: Thin and thinner: Sea ice mass balance measurements during SHEBA, J. Geophys. Res.-Oceans, 108, 1–21, https://doi.org/10.1029/2001JC001079, 2003.

Petrich, C., Eicken, H., Polashenski, C. M., Sturm, M., Harbeck, J. P., Perovich, D. K., and Finnegan, D. C.: Snow dunes: A controlling factor of melt pond distribution on Arctic sea ice, J. Geophys. Res.-Oceans, 117, C09029, https://doi.org/10.1029/2012JC008192, 2012.

Pirazzini, R., Hannula, H.-R., Shupe, M. D., Uttal, T., Cox, C. J., Costa, D., Persson, P. O. G., and Brasseur, Z.: Upward and downward broadband shortwave and longwave irradiance and downward diffuse and direct solar partitioning during the MOSAiC expedition, PANGAEA [data set], https://doi.org/10.1594/PANGAEA.952359, 2022.

Polashenski, C., Perovich, D., and Courville, Z.: The mechanisms of sea ice melt pond formation and evolution, J. Geophys. Res.-Oceans, 117, C01001, https://doi.org/10.1029/2011JC007231, 2012.

Rabe, B., Karcher, M., Schauer, U., Toole, J. M., Krishfield, R. A., Pisarev, S., Kauker, F., Gerdes, R., and Kikuchi, T.: An assessment of Arctic Ocean freshwater content changes from the 1990s to the 2006–2008 period, Deep-Sea Res. Pt. I, 58, 173–185, 2011.

Rabe, B., Cox, C. J., Fang, Y.-C., et al.: The MOSAiC Distributed Network: Observing the coupled Arctic system with multidisciplinary, coordinated platforms, Elementa: Science of the Anthropocene, 12, 1, https://doi.org/10.1525/elementa.2023.00103, 2024.

Raphael, I., Clemens-Sewall, D., Perovich, D., Polashenski, C., Itkin, P., Regnery, J., Nicolaus, M., Jaggi, M., Smith, M., Matero, I., Macfarlane, A., Hutchings, J., Jutila, A., Fons, S., Oggier, M., Wagner, D., and Demir, O.: Measurements of sea ice point-mass-balance using hotwire thickness gauges and ablation stakes during the Multidisciplinary drifting Observatory for the Study of Arctic Climate (MOSAiC) Expedition in the Central Arctic (2019–2020) [data set], https://doi.org/10.18739/A2NK36626, 2022.

Raphael, I. A., Perovich, D. K., Polashenski, C. M., Clemens-Sewall, D., Itkin, P., Lei, R., Nicolaus, M., Regnery, J., Smith, M. M., Webster, M., and Jaggi, M.: Sea ice mass balance during the MOSAiC drift experiment, Elementa: Science of the Anthropocene, 12, 00040, https://doi.org/10.1525/elementa.2023.00040, 2024.

Richter-Menge, J. A., Perovich, D. K., and Pegau, W. S.: Summer ice dynamics during SHEBA and its effect on the ocean heat content, Ann. Glaciol., 33, 201–206, 2001.

Salganik, E., Katlein, C., Lange, B. A., Matero, I., Lei, R., Fong, A. A., Fons, S. W., Divine, D., Oggier, M., Castellani, G., Bozzato, D., Chamberlain, E. J., Hoppe, C. J. M., Müller, O., Gardner, J., Rinke, A., Pereira, P. S., Ulfsbo, A., Marsay, C., Webster, M. A., Maus, S., Høyland, K. V., and Granskog, M. A.: Temporal evolution of under-ice meltwater layers and false bottoms and their impact on summer Arctic sea ice mass balance, Elem. Sci. Anth., 11, 00035, https://doi.org/10.1525/elementa.2022.00035, 2023a.

Salganik, E., Lange, B. A., Itkin, P., Divine, D., Katlein, C., Nicolaus, M., Hoppmann, M., Neckel, N., Ricker, R., Høyland, K. V., and Granskog, M. A.: Different mechanisms of Arctic first-year sea-ice ridge consolidation observed during the MOSAiC expedition, Elem. Sci. Anthr., 11, 00008, https://doi.org/10.1525/elementa.2023.00008, 2023b.

Salganik, E., Lange, B. A., Katlein, C., Matero, I., Anhaus, P., Muilwijk, M., Høyland, K. V., and Granskog, M. A.: Observations of preferential summer melt of Arctic sea-ice ridge keels from repeated multibeam sonar surveys, The Cryosphere, 17, 4873–4887, https://doi.org/10.5194/tc-17-4873-2023, 2023c.

Salganik, E., Hoppmann, M., Scholz, D., Arndt, S., Demir, O., Divine, D. V., Haapala, J., Hendricks, S., Itkin, P., Katlein, C., Kolabutin, N., Lei, R., Matero, I., Nicolaus, M., Raphael, I., Regnery, J., Oggier, M., Sheikin, I., Shimanchuk, E., and Spreen, G.: Temperature and heating induced temperature difference measurements from Digital Thermistor Chains (DTCs) during MOSAiC 2019/2020, PANGAEA [data set], https://doi.org/10.1594/PANGAEA.964023, 2023d.

Salganik, E., Crabeck, O., Fuchs, N., Hutter, N., Anhaus, P., and Landy, J. C.: Impacts of air fraction increase on Arctic sea-ice thickness retrieval during melt season, EGUsphere [preprint], https://doi.org/10.5194/egusphere-2024-2398, 2024.

Schulz, K., Mohrholz, V., Fer, I., Janout, M., Hoppmann, M., Schaffer, J., and Koenig, Z.: A full year of turbulence measurements from a drift campaign in the Arctic Ocean 2019–2020, Scientific Data, 9, 472, https://doi.org/10.1038/s41597-022-01574-1, 2022.

Schulz, K., Koenig, Z., Muilwijk, M., Bauch, D., Hoppe, C. J., Droste, E., Hoppmann, M., Chamberlain, E. J., Laukert, G., Stanton, T., Quintanilla-Zurita, A., Fer, I., Heuzé, C., Karam, S., Mieruch-Schnülle, S., Baumann, T. M., Vredenborg, M., Tippenhauer, S., and Granskog., M. A.: The Eurasian Arctic Ocean along the MOSAiC drift in 2019–2020: An interdisciplinary perspective on physical properties and processes, Elementa: Science of the Anthropocene, 12, 00114, https://doi.org/10.1525/elementa.2023.00114, 2024.

Sévellec, F., Fedorov, A. V., and Liu, W.: Arctic sea-ice decline weakens the Atlantic meridional overturning circulation, Nat. Clim. Change, 7, 604–610, 2017.

Shupe, M.: ShupeTurner cloud microphysics product, ARM Mobile Facility (MOS) MOSAiC (Drifting Obs – Study of Arctic Climate) [data set], https://doi.org/10.5439/1871015, 2022.

Shupe, M., Rex, M., Dethloff, K., Damm, E., Fong, A., Gradinger, R., Heuze, C., Loose, B., Makarov, A., Maslowski, W., Nicolaus, M., Perovich, D., Rabe, B., Rinke, A., Sokolov, V., and Sommerfeld, A.: The MOSAiC Expedition: A Year Drifting with the Arctic Sea Ice, Arctic Report Card, https://doi.org/10.25923/9g3v-xh92, 2020.

Shupe, M. D.: A ground-based multisensor cloud phase classifier, Geophys. Res. Lett., 34, L22809, https://doi.org/10.1029/2007GL031008, 2007.

Skyllingstad, E. D., Paulson, C. A., Pegau, W. S., McPhee, M. G., and Stanton, T.: Effects of keels on ice bottom turbulence exchange, J. Geophys. Res.-Oceans, 108, 3372, https://doi.org/10.1029/2002JC001488, 2003.

Smith, M., Bozzato, D., Chamberlain, E., Dietrich, U., Droste, E., Fong, A., Light, B., Linhardt, F., Matero, I., Perovich, D., Raphael, I., Regnery, J., Salganik, E., Tavri, A., von Albedyll, L., and Webster, M.: Near-surface ocean temperature & salinity measurements (using YSI and Castaway) during the summer component of the Multidisciplinary drifting Observatory for the Study of Arctic Climate (MOSAiC) campaign in the Central Arctic Ocean, July–September 2020, Arctic Data Center, https://doi.org/10.18739/A2TT4FV1G, 2021.

Smith, M. M., Holland, M., and Light, B.: Arctic sea ice sensitivity to lateral melting representation in a coupled climate model, The Cryosphere, 16, 419–434, https://doi.org/10.5194/tc-16-419-2022, 2022a.

Smith, M. M., von Albedyll, L., Raphael, I. A., Lange, B. A., Matero, I., Salganik, E., Webster, M. A., Granskog, M. A., Fong, A., Lei, R., and Light, B.: Quantifying false bottoms and under-ice meltwater layers beneath Arctic summer sea ice with fine-scale observations, Elem. Sci. Anth., 10, 000116, https://doi.org/10.1525/elementa.2021.000116, 2022b.

Smith, M. M., Angot, H., Chamberlain, E. J., Droste, E. S., Karam, S., Muilwijk, M., Webb, A. L., Archer, S. D., Beck, I., Blomquist, B. W., Bowman, J., Boyer, M., Bozzato, D., Chierici, M., Creamean, J., D'Angelo, A., Delille, B., Fer, I., Fong, A. A., Fransson, A., Fuchs, N., Gardner, J., Granskog, M. A., Hoppe, C. J. M., Hoppema, M., Hoppmann, M., Mock, T., Muller, S., Müller, O., Nicolaus, M., Nomura, D., Petäjä, T., Salganik, E., Schmale, J., Schmidt, K., Schulz, K., Shupe, M. D., Stefels, J., Thielke, L., Tippenhauer, S., Ulfsbo, A., van Leeuwe, M., Webster, M., Yoshimura, M., and Zhan, L.: Thin and transient meltwater layers and false bottoms in the Arctic sea ice pack – recent insights on these historically overlooked features, Elementa: Science of the Anthropocene, 11, 00025, https://doi.org/10.1525/elementa.2023.00025, 2023.

Solomon, A., Heuzé, C., Rabe, B., Bacon, S., Bertino, L., Heimbach, P., Inoue, J., Iovino, D., Mottram, R., Zhang, X., Aksenov, Y., McAdam, R., Nguyen, A., Raj, R. P., and Tang, H.: Freshwa-

ter in the Arctic Ocean 2010–2019, Ocean Sci., 17, 1081–1102, https://doi.org/10.5194/os-17-1081-2021, 2021.

Steiner, N., Holloway, G., Gerdes, R., Häkkinen, S., Holland, D., Karcher, M., Kauker, F., Maslowski, W., Proshutinsky, A., Steele, M., and Zhang, J.: Comparing modeled streamfunction, heat and freshwater content in the Arctic Ocean, Ocean Model., 6, 265–284, 2004.

Strub-Klein, L. and Sudom, D.: A comprehensive analysis of the morphology of first-year sea ice ridges, Cold Reg. Sci. Technol., 82, 94–109, 2012.

Sumata, H., de Steur, L., Divine, D. V., Granskog, M. A., and Gerland, S.: Regime shift in Arctic Ocean sea ice thickness, Nature, 615, 443–449, 2023.

Tao, R., Nicolaus, M., Katlein, C., Anhaus, P., Hoppmann, M., Spreen, G., Niehaus, H., Jäkel, E., Wendisch, M., and Haas, C.: Seasonality of spectral radiative fluxes and optical properties of Arctic sea ice during the spring–summer transition, Elementa: Science of the Anthropocene, 12, 00130, https://doi.org/10.1525/elementa.2023.00130, 2024.

Vancoppenolle, M., Fichefet, T., and Goosse, H.: Simulating the mass balance and salinity of Arctic and Antarctic sea ice. 2. Importance of sea ice salinity variations, Ocean Model., 27, 54–69, 2009a.

Vancoppenolle, M., Fichefet, T., Goosse, H., Bouillon, S., Madec, G., and Maqueda, M. A. M.: Simulating the mass balance and salinity of Arctic and Antarctic sea ice. 1. Model description and validation, Ocean Model., 27, 33–53, https://doi.org/10.1016/j.ocemod.2008.10.005, 2009b.

Webster, M. A., Rigor, I. G., Perovich, D. K., Richter-Menge, J. A., Polashenski, C. M., and Light, B.: Seasonal evolution of melt ponds on Arctic sea ice, J. Geophys. Res.-Oceans, 120, 5968–5982, 2015.

Webster, M. A., Holland, M., Wright, N. C., Hendricks, S., Hutter, N., Itkin, P., Light, B., Linhardt, F., Perovich, D. K., Raphael, I. A., Smith, M. M., von Albedyll, L., and Zhang, J.: Spatiotemporal evolution of melt ponds on Arctic sea ice: MOSAiC observations and model results, Elem. Sci. Anth., 10, 000072, https://doi.org/10.1525/elementa.2021.000072, 2022.

Zhang, Z., Hui, F., Shokr, M., Granskog, M. A., Cheng, B., Vihma, T., and Cheng, X.: Winter Arctic Sea Ice Surface Form Drag During 1999–2021: Satellite Retrieval and Spatiotemporal Variability, IEEE T. Geosci. Remote, 62, 4300420, https://doi.org/10.1109/TGRS.2023.3347694, 2024.